Research Square

Preprints are preliminary reports that have not undergone peer review.
They should not be considered conclusive, used to inform clinical practice,
or referenced by the media as validated information.

# Cold Plasma-Engineered CNPs/TiO2 /CuO/Chitosan Nanocomposite for Cadmium Adsorption: Optimization, Isotherms, Kinetics, and Selectivity

**Mehrnaz Akhundi Nematzadeh**
SR.C, Islamic Azad University
**Sahar Baniyaghoob**
baniyaghoob@iau.ac.ir
SR.C, Islamic Azad University
**Shahrooz Saviz**
SR.C, Islamic Azad University
**Reza Fazaeli**
Islamic Azad University South Tehran Branch

**Article**

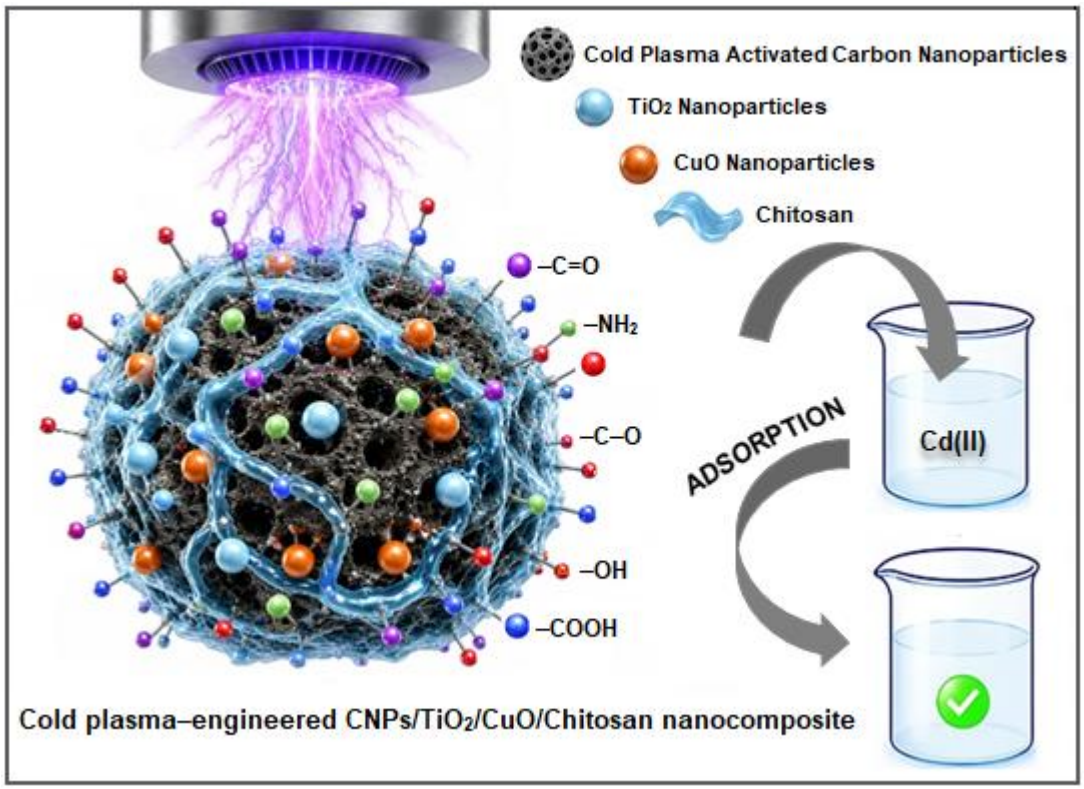
**Keywords:** Cold plasma-engineering, Chitosan, Cd(II) adsorption, Selectivity, Wastewater treatment

**Posted Date:** November 10th, 2026

**DOI:** https://doi.org/10.21203/rs.3.rs-11447440/v1

**License:** This work is licensed under a Creative Commons Attribution 4.0 International License.
Read Full License

**Additional Declarations:** No competing interests reported.




**Graphical Abstract**

## Highlights

- Cold plasma–engineered CNPs/$TiO_2$/CuO/Chitosan nanocomposite synthesized.
- Optimized via Response Surface Methodology (RSM).
- Achieved 91.98% Cd(II) adsorption efficiency; max capacity reached 120.45 mg $g^{-1}$.
- Adsorption followed pseudo-second-order kinetics and the Freundlich isotherm.
- High performance and structural integrity across five adsorption-desorption cycles.

# Cold Plasma-Engineered CNPs/$TiO_2$/CuO/Chitosan Nanocomposite for Cadmium Adsorption: Optimization, Isotherms, Kinetics, and Selectivity

Mehrnaz Akhundi Nematzadeh [a], Sahar Baniyaghoob [a*], Shahrooz Saviz [a], Reza Fazaeli [b]

[a] *Department of Chemistry, SR.C., Islamic Azad University, Tehran, Iran*

[b] *Department of Chemistry, South Tehran Branch, Islamic Azad University, Tehran, Iran*

[*] *Corresponding author: Tel.: +98 912 335 20 46; e-mail address: baniyaghoob@iau.ac.ir*

**ABSTRACT**

This study reports the fabrication of a cold plasma–engineered CNPs/$TiO_2$/CuO/Chitosan nanocomposite for effectively sequestering cadmium (Cd(II)) ions from aqueous media. The green cold-plasma synthesis approach simultaneously integrated multiple functional groups onto carbon nanoparticles (CNPs), generating a highly active heterogeneous surface. Applied to the ternary $TiO_2$/CuO/Chitosan system, the nanocomposite delivered superior adsorption performance. Response surface methodology (RSM) optimized key process parameters: initial Cd(II) concentration at 68.62 mg $L^{-1}$, nanocomposite dosage at 26.20 mg, pH 6.89, and contact time of 79 min. Analysis of variance (ANOVA) confirmed the statistical significance of these variables and their interactions. Under these optimized conditions, the nanocomposite achieved a 91.98% adsorption efficiency. Kinetic analysis followed a pseudo-second-order mechanism, while isotherm data aligned well with the Freundlich model, suggesting multilayer adsorption. The nanocomposite's selectivity in binary systems containing Pb(II) ions was also evaluated. In single-component systems, equilibrium capacities reached 120.45 mg $g^{-1}$ and 99.75 mg $g^{-1}$ for Cd(II) and Pb(II), respectively. In binary matrices, these capacities decreased to 85.65 mg $g^{-1}$ and 50.35 mg $g^{-1}$, and the selectivity coefficient (αCd/Pb) peaked at 4.58 (pH 6.5). Reusability studies confirmed the nanocomposite's structural and chemical stability, retaining 87.25% of its adsorption efficiency after five successive acidic desorption cycles. These findings demonstrate that the cold plasma-engineered CNPs/$TiO_2$/CuO/Chitosan nanocomposite is a robust, efficient, and environmentally friendly candidate for sustainable wastewater treatment applications.

***Keywords***

Cold plasma-engineering, Chitosan, Cd(II) adsorption, Selectivity, Wastewater treatment

## 1. Introduction

Environmental contamination degrades natural ecosystems, often caused by pollutants that exceed ecological tolerance limits [1]. These contaminants are broadly classified as biological, organic, and inorganic [2]. Biological pollution primarily involves pathogens and allergens, while organic pollutants include natural and

synthetic substances such as animal waste, agricultural residues, polychlorinated biphenyls, and polyaromatic hydrocarbons [3]. Inorganic contamination, especially heavy metal contamination in aquatic environments, has become a major public health concern. Heavy metals originate from natural processes and human activities, including leather tanning, battery manufacturing, steel production, food processing, pigment synthesis, and agricultural chemicals such as fertilizers and pesticides [4]. The entry of heavy metals, specifically cadmium (Cd(II)), lead (Pb(II)), mercury (Hg(II)), and arsenic (As(III)), into wastewater systems poses a severe global threat. Their toxicity is linked to physicochemical properties, notably high atomic mass, electronegativity, and affinity for forming stable complexes with vital biological molecules, which collectively lead to enzyme inhibition, genomic damage, and metabolic dysregulation. Cd(II) and Pb(II) are particularly hazardous because they are non-biodegradable, highly bioaccumulative, and carcinogenic, even at trace concentrations [5]. Chronic exposure disrupts calcium-dependent neurotransmission and synaptic function, triggers oxidative stress, nephrotoxicity, and bone demineralization, often by displacing essential divalent cations like zinc and calcium in metalloproteins, and elevates mortality risks in vulnerable populations [6]. These concerns emphasize the urgent necessity for advanced remediation strategies. Conventional water treatment technologies, including ion exchange, coagulation-flocculation, membrane filtration, reverse osmosis, and chemical precipitation, are often constrained by incomplete removal efficiency, high operational costs, and the generation of secondary pollutants [7, 8]. In response, research interest has shifted toward nanotechnology-based adsorption systems for selective sequestration of heavy metals from complex aqueous matrices, offering advantages such as a high surface-to-volume ratio, tunable surface chemistry, operational simplicity, and superior adsorption capacity [9]. Recent advances highlight the role of surface engineering and the rational design of functionalized nanomaterials through the strategic incorporation of chelating groups [10].

Among nanomaterials, carbon nanoparticles (CNPs) show exceptional potential because of unique physicochemical properties, including high specific surface area, crystallinity, excellent chemical stability, and well-defined stoichiometry [11]. However, they suffer from aggregation, limited adsorption capacity, lack of selectivity, and poor recovery from aqueous media [12]. To address these limitations, surface functionalization has emerged as a critical strategy. Dielectric barrier discharge cold plasma (DBD-CP) offers an innovative solution to these constraints [13, 14]. DBD-CP is a clean, solvent-free, and tunable technique for surface engineering that improves particle dispersion, surface roughness, electronic structure, and adsorption capacity [15, 16]. This non-thermal plasma, composed of ions, radicals, and UV photons, generates abundant oxygen-containing functional groups without disrupting the carbon framework [17]. These functional groups facilitate electrostatic attraction and surface complexation with metal species and enhance binding affinity through tailored coordination [18]. DBD-CP modulates the spatial arrangement and density of functional groups to balance the distribution of selective binding sites. This is accomplished by integrating synergistic complementary groups, such as hydroxyl (–OH), carboxyl (–COOH), and carbonyl (–C=O), onto a single, non-selective binding platform

[19]. For instance, the synergistic effect between amino and carboxyl groups enables preferential binding based on coordination-geometry preferences in complex multi-component systems. Amino groups primarily act as Lewis bases, donating nitrogen lone pairs to enhance the uptake of soft metal ions [20]. In contrast, carboxyl groups function as Brønsted acids, facilitating electrostatic interactions to capture cationic species [21]. Moreover, the pH-dependent speciation of surface functional groups and metal ions governs adsorption performance. Protonation of amino groups at low pH and deprotonation of carboxyl groups under alkaline conditions directly modulate their metal-binding affinities and adsorption capacities [22].

The cooperative effects of surface functional groups are evident in chitosan because of its abundant, accessible $–NH_2$ and –OH groups. Qu et al. (2023) efficiently removed toxic Cr(VI) ions from real wastewater using chitosan-modified magnetic carbon nanomaterials [23]. Chitosan, a deacetylated derivative of chitin, is a linear polysaccharide known for its low toxicity, bioactivity, biocompatibility, and biodegradability [24]. In nanocomposite systems, chitosan forms a three-dimensional network; however, it may suffer from mechanical instability and susceptibility to degradation under varying pH and temperature conditions. Therefore, its practical implementation in water treatment applications may be limited [25].

In response, metal oxide nanoparticles, such as titanium dioxide ($TiO_2$) and copper oxide (CuO), have emerged as compelling alternatives and have garnered significant attention for their efficacy in heavy-metal sequestration and versatility in advanced water treatment applications [26]. The high performance of metal oxides stems from their chemically active surface architecture [27]. Abundant surface hydroxyl groups enable highly specific coordination chemistry through inner-sphere complexation. As a result, the metal oxide surface interacts precisely with target metal ions, driven by the interplay between the ion's hydration energies and the surface's Lewis acidity/basicity [28]. Consequently, these oxides achieve superior selectivity by favoring specific metal-ligand bond strengths over non-specific, long-range electrostatic attractions [29].

In this study, we synthesized surface-engineered CNPs decorated with $TiO_2$ and CuO nanoparticles and encapsulated in chitosan as an effective nanocomposite for Cd(II) sequestration from aqueous solutions. The simultaneous integration of oxygen-mediated chelation groups, supported by a green, sustainable cold plasma approach, created a heterogeneous surface environment that overcame the inherent limitations of selective Cd(II) adsorption. This research examined the mechanisms governing cooperative interactions between surface chemistry and metal-ion coordination preferences through experimental characterization and computational modeling. Expected outcomes included developing predictive models for maximum Cd(II) adsorption. The response surface methodology (RSM) was employed to optimize operational parameters for Cd(II) adsorption, including initial Cd(II) concentration, nanocomposite dosage, solution pH, and contact time, even under challenging conditions such as high Cd(II) concentrations and minimal nanocomposite loading. Analysis of Variance (ANOVA) assessed the influence of these parameters. Furthermore, the kinetics and adsorption isotherms were analyzed to propose a fundamental theoretical framework for Cd(II) adsorption behavior. The

cold plasma–engineered CNPs/$TiO_2$/CuO/Chitosan nanocomposite, accommodating diverse coordination geometries and binding preferences, was used in a competitive binary system to evaluate potential synergistic or antagonistic interactions between Cd(II) and Pb(II) ions. Finally, comprehensive characterization using X-ray diffraction (XRD), Fourier-transform infrared spectroscopy (FTIR), X-ray photoelectron spectroscopy (XPS), Brunauer–Emmett–Teller (BET) analysis, Zeta potential analysis, field-emission scanning electron microscopy (FESEM), energy-dispersive X-ray spectroscopy (EDX), and transmission electron microscopy (TEM) confirmed the successful formation of the well-integrated nanocomposite, which exhibited consistent performance across multiple adsorption-desorption cycles in reusability tests.

## 2. Experimental

### *2.1. Materials*

All chemicals were purchased from Sigma-Aldrich International GmbH (Germany) as analytical grade. Pure carbon nanoparticles (molecular weight 12.01 g $mol^{-1}$, BET surface area >100 $m^2$ $g^{-1}$, and size <100 nm by TEM) were used as the core material of the nanocomposite. White to beige chitosan flakes, derived from shrimp shells, were prepared with a deacetylation degree of ≥75%. Chemicals including cadmium nitrate tetrahydrate ($Cd(NO_3)_2 \cdot 4H_2O$, 308.48 g $mol^{-1}$), titanium(IV) isopropoxide (TTIP, Ti $(OCH(CH_3)_2)_4$, 284.22 g $mol^{-1}$), copper(II) acetate monohydrate ($Cu(CH_3COO)_2 \cdot H_2O$, 241.60 g $mol^{-1}$), potassium hydroxide (KOH, 56.10 g $mol^{-1}$), glacial acetic acid ($CH_3COOH$, 60.05 g $mol^{-1}$), and ethanol ($C_2H_6O$, 46.07 g $mol^{-1}$) were used without further purification.

### *2.2. Synthesis of the cold plasma-engineered CNPs/$TiO_2$/CuO/Chitosan nanocomposite*

The cold plasma–engineered CNPs/$TiO_2$/CuO/Chitosan nanocomposite was synthesized via a four-step procedure (Fig. 1):

**Step 1:** The CNPs were initially surface-modified using a dielectric barrier discharge cold plasma source with air as the working gas. The discharge was sustained at an applied voltage of 10 kV and a current of 30 mA, with an electrode gap of 2 cm and a gas flow rate of 5 L $min^{-1}$. The treatment was maintained for 1 h to ensure effective surface functionalization.

**Step 2:** The plasma-activated CNPs (1 g) were dispersed in 50 mL of ethanol via ultrasonication for 60 min. TTIP (35 mL) was then added dropwise to the suspension under acidic conditions (pH ≈ 2) to facilitate the in situ loading of 7 wt.% $TiO_2$ relative to the carbon support. Following an aging period, the precipitate was washed, oven-dried at 80°C for 5 h, and calcined at 400°C under a nitrogen ($N_2$) atmosphere for 3 h.

**Step 3:** The $TiO_2$-modified product was dispersed in 40 mL of deionized (DI) water for 60 min. Separately, copper(II) acetate monohydrate (0.12 g) was dissolved in 20 mL of DI water and added to the suspension. The pH of the mixture was adjusted to ≈ 10 using a KOH solution to promote the in situ precipitation of 4 wt.% CuO

species. After aging, the resulting material was washed, dried at 80°C for 5 h, and calcined at 250°C under a pure $N_2$ atmosphere for 2 h.

**Step 4:** The CuO-modified product was dispersed in 35 mL of DI water for 60 min. Simultaneously, chitosan (0.08 g) was dissolved in 30 mL of 1% (v/v) acetic acid solution under stirring at 40°C for 2 h. The modified product was added to the chitosan solution and stirred for 12 h, yielding a final chitosan content of 8 wt.%. The mixture was subjected to hydrothermal treatment at 150°C for 6 h, followed by thorough washing and drying at 80°C for 12 h. Finally, the cold plasma–engineered CNPs/$TiO_2$/CuO/Chitosan nanocomposite was stored in a cool, dry place.

**→ Fig. 1 ←**

### *2.3. Characterization*

XRD analysis was carried out on a PHILIPS X'PERT PRO X-ray diffractometer using Cu-Kα radiation (λ=1.54 Å) with a scanning angle (2θ) from 10° to 80°. FT-IR spectra were recorded on a SHIMADZU IR Prestige-21 IR spectrophotometer within the 4000-500 $cm^{-1}$ range. XPS spectra were acquired with a BESTEC EA 10 spectrometer with a monochromatic Al-Kα source. The BET specific surface area was collected at -196 °C on a BELSORP MINI II apparatus by nitrogen adsorption-desorption isotherms. Zeta potential analysis was performed using a HORIBA Scientific SZ-100 at 25°C. FESEM images and EDX data were obtained using a MIRA III VEGA-TESCAN-XMU instrument. TEM images were recorded with a PHILIPS CM 120 apparatus. Throughout the study, the concentration of Cd(II) ions in the aqueous solutions was determined using atomic absorption spectroscopy (AAS) with a Varian AA240 instrument.

### *2.4. Adsorption experiments*

A stock solution of cadmium (1000 mg $L^{-1}$) was prepared by dissolving cadmium nitrate tetrahydrate in DI water and storing it in the dark at 4°C. Cadmium ions remain divalent over a broad pH range because they have a low tendency toward hydrolysis [30]; however, a small amount of 0.1 N nitric acid was added to stabilize the solution and prevent Cd(II) precipitation. Working solutions of 20 mg $L^{-1}$ to 100 mg $L^{-1}$ were then prepared by serial dilution. In a typical adsorption experiment, a specified mass of the nanocomposite (10- 50 mg) was dispersed in 50 mL of Cd(II) working solution. The initial pH was adjusted to 5.5- 7.5 using dilute HCl or NaOH. The mixture was stirred at room temperature for predetermined contact times (30- 150 min). In each experiment, the suspension was filtered, and the residual Cd(II) concentration was quantified using an AAS. Blank experiments without nanocomposite were also conducted across the pH range to confirm the Cd(II) chemical behavior. The Cd(II) adsorption efficiency (R, %) and equilibrium adsorption capacity (qe, mg $g^{-1}$) were calculated as follows:

$$R = ((C_0 - C_t) / C_0)_x 100 \quad (1)$$

$$qe = (C_0 - C_t) V / M \quad (2)$$

where $C_0$ and $C_t$ (mg $L^{-1}$) are the initial and time-dependent Cd(II) concentrations at time t (min), respectively; V (L) is the solution volume, and M (g) is the mass of the adsorbent used [28].

### *2.5. Response Surface Methodology*

Cd(II) adsorption performance was evaluated using response surface methodology (RSM) based on design of experiments (DOE). Unlike traditional One-Variable-at-a-Time (OVAT) methods, which are labor-intensive, costly, and overlook interactions among variables, RSM examines multiple variables simultaneously. This approach improves efficiency and reduces costs and reagent use. RSM models and analyzes interactions between parameters, offering a thorough understanding of the process [27]. In this study, central composite design (CCD), a robust and widely used RSM component, was employed to estimate quadratic response surfaces and develop second-order polynomial models describing the relationship between input and output variables. A key advantage of CCD is the inclusion of axial points (-α and +α) within the experimental domain, which improves model robustness and predictive accuracy across varying operating conditions. A five-level CCD was implemented for four independent variables: initial Cd(II) concentration, nanocomposite dosage, solution pH, and contact time (Table 1). By default, high factor levels were coded as +1 and low levels as -1. The relationship between these independent variables and the response variable, defined as the Cd(II) adsorption efficiency (Y), was modeled using the following second-order polynomial equation:

$$Y = \beta 0 + \sum_{i=1}^{k} \beta i \, Xi + \sum_{i=1}^{k} \beta ii \, X_i^2 + \sum_{i=1}^{k} \sum_{j=i+1}^{k} \beta ij \, Xi \, Xj + \varepsilon \quad (3)$$

Here, Y denotes the predicted response; β0 represents the intercept coefficient; βi, βii, and βij are the regression coefficients for the linear, quadratic, and interaction effects, respectively; Xi and Xj denote the coded independent variables; and ε represents the random error [29]. The optimization procedure involved estimating these coefficients, predicting the response values, and performing diagnostic checks to validate the model's statistical adequacy.

**→ Table 1 ←**

### *2.6. Kinetics and adsorption isotherms*

Adsorption kinetics are commonly evaluated using the pseudo-second-order model, which implies that the rate-limiting step is governed by chemical interactions (chemisorption) between the adsorbent and the adsorbate. The following equation expresses it:

$$t / qt = 1 / K_2 \, qe^2 + 1 / qe \, (t) \quad (4)$$

where qe (mg $g^{-1}$) represents the equilibrium adsorption capacity, qt (mg $g^{-1}$) is the adsorption capacity at time t (min), and $K_2$ (g $mg^{-1}$ $min^{-1}$) is the pseudo-second-order kinetic constant. The $K_2$ and qe parameters are determined by linear regression of t / qt versus t, where the slope and intercept correspond to 1 / qe and 1 / $K_2$ $qe^2$, respectively [31].

In solid-liquid systems, adsorption involves the accumulation and concentration of one or more solution components onto a solid surface until equilibrium is reached. This equilibrium state is characterized by qe and Ce, and adsorption isotherms describe their relationship. qe (mg $g^{-1}$) is defined as the amount of adsorbate per unit mass of sorbent, while Ce (mg $L^{-1}$) represents the equilibrium concentration of the remaining adsorbate in the solution. The Langmuir and Freundlich isotherms are the most widely used models because they fit adsorption data well.

The Langmuir isotherm assumes monolayer adsorption on a homogeneous surface with a finite number of identical, energetically equivalent active sites. The following equation expresses it:

$$qe = qmax\, K_L\, Ce / 1 + K_L\, Ce \quad (5)$$

where qmax (mg $g^{-1}$) is the maximum adsorption capacity, and $K_L$ (L $mg^{-1}$) is the Langmuir constant related to binding-site affinity and adsorption energy [32].

The Freundlich isotherm model assumes heterogeneous adsorption on a surface with a non-uniform distribution of active sites and varying adsorption energies. It is commonly expressed in its linear form as:

$$\log qe = \log K_F + 1/n \log Ce \quad (6)$$

where $K_F$ (L $mg^{-1}$) is the Freundlich constant related to adsorption capacity, and n is the Freundlich exponent associated with adsorption intensity and surface heterogeneity [33].

### *2.7. Selectivity experiments*

The selectivity of the cold plasma–engineered CNPs/$TiO_2$/CuO/Chitosan nanocomposite was evaluated in the presence of competing Pb(II) ions. After optimizing Cd(II) adsorption, the same experimental parameters were applied to Pb(II) to determine its individual adsorption capacity. The Cd(II)-Pb(II) binary system was subsequently investigated at an equimolar (1:1) concentration ratio to evaluate competitive adsorption behavior and elucidate the potential synergistic or antagonistic interactions. The selectivity coefficient (α), quantifying the competitive adsorption, was determined using the following equation:

$$\alpha\,(A / B) = (q_{e,}\, A \,.\, C_e,\, B) / (q_{e,}\, B \,.\, C_e,\, A) \quad (7)$$

where A and B denote Cd(II) and Pb(II), respectively [31].

## 3. Results and discussion

### *3.1. Structural analysis*

The crystallographic structure of the cold plasma–engineered CNPs and the cold plasma–engineered CNPs/$TiO_2$/CuO/Chitosan nanocomposite, using XRD diffraction patterns, are compared in Fig. 2. Nanocrystalline CNPs in both XRD patterns show a prominent peak centered at 26.80°, originating from the (002) reflection, and a secondary peak at 43.40°, corresponding to the (100) reflection, align perfectly with *JCPDS* card *No*. 41-1487. These peaks confirm the crystalline nature and quasi-graphitic structure of the carbon nanoparticles, demonstrating that cold plasma surface modification effectively induced a more ordered, denser crystalline arrangement within the carbon lattice. The XRD pattern of the nanocomposite exhibits a high-intensity peak at 25.20°, corresponding to the (101) diffraction plane of the anatase phase of $TiO_2$ (*JCPDS* card *No*. 21-1272). The reflection observed at 27.40° corresponds to the (110) plane of the rutile phase (*JCPDS* card *No*. 21-1276). It is worth noting that the reflections from CNPs and $TiO_2$ partially overlap within the 25° to 28° diffraction angle range. In the XRD pattern of the nanocomposite, distinct peaks are observed at 38.97° and 48.74°, which are well indexed to the (200) and (202) planes of the CuO phase (*JCPDS* card *No*. 80-1268). The sharpness of these reflections confirms the high crystallinity of the CuO. The coexistence of these peaks alongside $TiO_2$ phases provides strong evidence for the formation of a multi-component heterogeneous structure. Additionally, the distinct reflection at 22.21° is attributed to the ordered arrangement of chitosan polymer chains, likely due to extensive intermolecular hydrogen bonding. It can be inferred that the interaction between the functional groups of chitosan and the metal oxides has caused broadening of the chitosan peak. The absence of any additional peaks associated with impurities indicates the high purity of the nanocomposite. To estimate the crystallite size, the Debye-Scherrer equation is used:

$$D = K \lambda / \beta \cos \theta \quad (8)$$

where D is the crystallite size (nm), K is a constant of 0.94, $\lambda$ is the X-ray radiation wavelength (0.15418 nm), $\beta$ is the full width at half maximum (FWHM) of the peaks (radians), and $\theta$ is the diffraction angle (radians) [33]. The average crystallite size of the cold plasma–engineered CNPs/$TiO_2$/CuO/Chitosan nanocomposite was determined to be 28 nm.

**→ Fig. 2 ←**

### *3.2. Chemical analyses*

Fig. 3 presents the chemical structure and functional groups of the cold plasma–engineered CNPs and the cold plasma–engineered CNPs/$TiO_2$/CuO/Chitosan nanocomposite. The FTIR spectra of both samples show a striking resemblance. This similarity confirms that the oxygen- and nitrogen-containing functional groups introduced via the cold plasma process remained unchanged during the nanocomposite fabrication. Strong bonding between the nanocomposite components eliminated transient spectral features, resulting in a unified, integrated structure that preserves the intrinsic characteristics of the CNPs. The presence of absorption bands

associated with $TiO_2$ and CuO indicates that the metal oxide nanoparticles have formed chemical bonds with functional groups derived from the cold plasma and do not readily detach from the nanocomposite matrix. This confirms the successful nanocomposite synthesis and accounts for its long-term stability. Shifts in absorption bands and changes in vibrational frequencies result from hydrogen bonding between functional groups and electrostatic interactions. Shifts in oxygen-containing groups, such as carbonyls, indicate that these groups act as ligands and entrap the metal oxides. The absorption bands at 524 $cm^{-1}$, 670 $cm^{-1}$, and 780 $cm^{-1}$ are assigned to Cu–O stretching vibrations, Ti–O–Ti vibrations, and N–H bending vibrations, respectively [34]. A distinct band at 1090 $cm^{-1}$ corresponds to C–H and C–C bending vibrations and C–N stretching vibrations [35]. Absorption bands at 1385 $cm^{-1}$ and 1460 $cm^{-1}$ are attributed to $CH_2$ bending vibrations [36]. A distinct absorption band at 1540 $cm^{-1}$ corresponds to N–H bending coupled with C–N stretching [37]. Absorption bands observed at 1650 $cm^{-1}$ and 1710 $cm^{-1}$ correspond to C=O stretching vibrations of carboxyl and amide carbonyl groups, indicating the presence of both functional groups on the nanocomposite surface [38]. Additionally, peaks at 2850 $cm^{-1}$ and 2950 $cm^{-1}$ correspond to symmetric and asymmetric C–H stretching vibrations. A broad absorption band at 3420 $cm^{-1}$ is attributed to O-H stretching vibrations from physically adsorbed water and to N-H stretching vibrations. Absorption bands in the 3744 $cm^{-1}$ and 3854 $cm^{-1}$ regions may correspond to symmetric and asymmetric N-H stretching vibrations [34].

**→ Fig. 3 ←**

Fig. 4a shows the elemental composition of the cold plasma–engineered CNPs/$TiO_2$/CuO/Chitosan nanocomposite, determined by EDX. The results confirm the presence of the constituent elements, C, N, O, Ti, and Cu, at their respective characteristic energy levels. Notably, the nitrogen signal is attributed to the amine functional groups inherent to the chitosan component, confirming its successful integration into the nanocomposite framework. This analysis shows no significant signal indicating potential impurities from the synthesis process. The inset shows the weight and atomic percentages of the constituent elements.

**→ Fig. 4 ←**

The elemental composition and surface chemical states of the cold plasma–engineered CNPs/$TiO_2$/CuO/Chitosan nanocomposite were analyzed using XPS over a binding energy range of 0 to 1200 eV. The survey spectrum (Fig. 4b) exhibits characteristic photoelectron lines at 285 eV, 460 eV, 531 eV, and 950 eV, corresponding to C 1s, Ti 2p, O 1s, and Cu 2p, respectively. Upon deconvolution, the C 1s spectrum (Fig. 4c) can be fitted into two primary peaks at 284.13 eV and 286.14 eV, attributed to the $sp^2$-hybridized graphitic C=C bonds and C–O or C–N functionalities, respectively. The latter confirms the presence of

oxygenated and nitrogenous species derived from chitosan [39]. The Ti 2p spectrum (Fig. 4d) displays two prominent peaks at 458.61 eV and 464.45 eV, corresponding to the Ti $2p_{3/2}$ and Ti $2p_{1/2}$, respectively. The measured binding energy separation of ~5.8 eV is consistent with the $Ti^{4+}$ oxidation state in $TiO_2$ [40]. The high-resolution O 1s spectrum (Fig. 4e) shows two distinct components at 530.25 eV and 532.62 eV, corresponding to lattice oxygen in the $TiO_2$ and CuO crystalline phases and adsorbed surface hydroxyl groups, respectively, indicating a rich oxygenated surface environment. Finally, the Cu 2p spectrum (Fig. 4f) exhibits two well-defined peaks at 933.68 eV and 953.55 eV, corresponding to the Cu $2p_{3/2}$ and Cu $2p_{1/2}$, respectively. The emergence of intense shake-up satellite peaks, a typical characteristic of the $d^9$ electron configuration, unambiguously confirms the $Cu^{2+}$ oxidation state in CuO, distinguishing it from metallic $Cu^0$ or $Cu^+$ species [41].

### *3.3. BET surface area*

The $N_2$ adsorption-desorption isotherms of the cold plasma–engineered CNPs and the cold plasma–engineered CNPs/$TiO_2$/CuO/Chitosan nanocomposite illustrate a typical Type I profile, in accordance with IUPAC classification (Fig. 5a). The sharp uptake at low relative pressures ($P/P_0$) signifies the dominant presence of the micropore filling process. At these very low pressures, the pores fill rapidly due to strong interactions between the narrow pore walls and the gas molecules; subsequently, saturation is reached, and the curve extends parallel to the relative pressure axis. The isotherm for purely microporous materials lacks a hysteresis loop, with adsorption and desorption curves that overlap, as observed in the nanocomposite. However, for CNPs, the H4 hysteresis loop indicates a hierarchical pore structure comprising both micropores and mesopores, attributed to capillary condensation within slit-like pores; the micropores provide high adsorption capacity, while the mesopores create access pathways [42]. The BET-specific surface areas of cold-plasma-engineered CNPs and the cold-plasma-engineered CNPs/$TiO_2$/CuO/Chitosan nanocomposite were calculated to be 2568.30 $m^2\ g^{-1}$ and 872.79 $m^2\ g^{-1}$, respectively, while their monolayer adsorption capacities ($V_m$) were determined to be 590.08 $cm^3$ (STP) $g^{-1}$ and 200.53 $cm^3$ (STP) $g^{-1}$, respectively. The reduction in the nanocomposite's surface area is primarily attributed to encapsulation and pore-blocking by the long-chain chitosan matrix, physical occupation of micropores/mesopores by the anchored $TiO_2$/CuO nanoparticles, and the higher mass density of the incorporated metal oxides. Carbon nanoparticles have a porous structure, and their surface area increases upon plasma exposure. However, chitosan is a polymeric macromolecule characterized by long, flexible chains. During nanocomposite formation, chitosan chains coat the surface of the CNPs, blocking a significant portion of the micropores and mesopores. Consequently, nitrogen gas cannot access the internal cavities, reducing surface area. Furthermore, polymer network formation and interactions between chitosan and the carbon nanoparticles during synthesis and drying induce structural compaction and chain entanglement, reducing free pore volume. In contrast, $TiO_2$/CuO nanoparticles nucleate and anchor at the pores and structural defects of the CNPs; because they have a higher mass density than carbon, they fill the material's pores and voids.

Fig. 5b displays the pore size distribution and porosity curves obtained using the Barrett, Joyner, and Halenda (BJH) method. The average pore diameters for the cold-plasma-engineered CNPs and the cold-plasma-engineered CNPs/$TiO_2$/CuO/Chitosan nanocomposite were calculated to be 2.04 nm and 2.03 nm, respectively, while the total pore volumes were determined to be 0.4591 $cm^3 g^{-1}$ and 0.1406 $cm^3 g^{-1}$, respectively. Interestingly, while the specific pore volume of the nanocomposite decreased by approximately 50% compared to the pristine plasma-modified CNPs, the average pore diameter remained largely unchanged. This behavior indicates that the intrinsic pore structure of the CNPs was preserved during the nanocomposite synthesis. The reduction in pore volume is attributed to the void-filling effect, where the incorporation of $TiO_2$/CuO nanoparticles and the chitosan matrix partially occupies the pre-existing pore channels without inducing structural collapse or altering pore geometry. This suggests that the remaining accessible pore network retains the characteristic size distribution of the plasma-engineered CNPs, confirming that the synthesis route successfully preserves the structural integrity of the carbonaceous support.

**→ Fig. 5 ←**

### *3.4. Zeta potential*

Nanoparticle dispersion in aqueous media can protonate or deprotonate surface OH groups, yielding $OH^{2+}$ or $O^-$ species, respectively; Zeta potential analysis characterizes this surface charge state. A Zeta potential magnitude exceeding 30 mV typically indicates high colloidal stability due to electrostatic repulsion. As illustrated in Fig. 5c, the nanocomposite exhibits a mean Zeta potential of −35.9 mV at pH ~7, confirming the long-term stability of the strongly anionic nanoparticles. This strong negative surface charge facilitates adsorption of Cd(II) ions via electrostatic attraction.

### *3.5. Morphological studies*

FESEM examined the surface morphology of the cold plasma–engineered CNPs/$TiO_2$/CuO/Chitosan nanocomposite, as shown in Fig. 6(a-d). The micrographs reveal an irregular, highly porous morphology, suggesting successful integration of metal oxide nanoclusters into the chitosan and the modified CNPs framework. In fractured regions, pulled-out metal-oxide nanoparticles create crack-bridging features that impede crack initiation and propagation. Moreover, the coexistence of coalesced quasi-spherical particles and localized interfacial defects increases the effective surface-area-to-volume ratio, which is highly advantageous for Cd(II) ion adsorption. The particle size distribution curve (Fig. 6e) shows an average diameter of 20.60 nm.

TEM was employed to resolve the internal architecture of the nanocomposite, as shown in Fig. 6(f-i). The micrographs show distinct morphological heterogeneity: dark gray regions correspond to the CNPs, while the bright, smooth areas correspond to the chitosan, both appearing as thin, transparent layers. Notably, highly

dispersed black spherical nanoparticles are identified as the metal oxide component, forming small clusters with an average diameter of 8.68 nm (Fig. 6j). Furthermore, no free nanoparticles are observed outside the composite matrix, signifying a highly homogeneous dispersion. This tight interfacial integration is attributed to strong hydrogen bonding between the surface hydroxyl groups of the metal-oxide nanoparticles and the functional moieties of chitosan, minimizing interparticle distance and ensuring the structural integrity of the nanocomposite.

**→ Fig. 6 ←**

### *3.6. Adsorption*

#### *3.6.1. Statistical assessment*

In this study, a CCD model within the RSM framework was employed to systematically evaluate the adsorption efficiency of the cold plasma–engineered CNPs/$TiO_2$/CuO/Chitosan nanocomposite. An experimental matrix comprising 30 runs (Table 2) investigated the interactions among four critical independent variables: (A) initial Cd(II) concentration, (B) nanocomposite dosage, (C) solution pH, and (D) contact time. Based on ANOVA and statistical regression, the optimal quadratic model describing Cd(II) adsorption efficiency (R) in terms of coded factors is expressed as follows:

$$R\ (\%) = 88.54 + 4.34\ A + 4.13\ B + 3.14\ C + 1.87\ D + 1.31\ AB - 0.1706\ AC + 0.3606\ AD - 3.48\ BC - 2.35\ BD - 3.51\ CD - 0.5720\ A^2 - 7.40\ B^2 + 1.66\ C^2 + 1.06\ D^2 \quad (9)$$

**→ Table 2 ←**

ANOVA verified the adequacy, reliability, and predictive capability of the developed quadratic model, as summarized in Table 3. The model was highly significant, with an F-value of 378.93, a P-value of <0.0001, and a sum of squares of 3486.63, indicating that it describes Cd(II) adsorption as a function of the selected parameters. The correlation coefficients support the goodness of fit: an $R^2$ value of 0.9972 indicates that the model accounts for 99.72% of the total variance in the experimental data. The proximity of the Adjusted $R^2$ (0.9945) and Predicted $R^2$ (0.9856) values demonstrates model robustness and confirms no overfitting.

Adequate Precision: The signal-to-noise ratio was 88.52, well above the threshold for a reliable design space. The Lack of Fit (LOF) term was non-significant ($F = 2.74$, $p > 0.05$), indicating that the regression equation adequately represents the relationship between the experimental variable and the response. Experimental reproducibility was evidenced by a low Coefficient of Variation (C.V.%) of 0.96%, a standard deviation (Std. Dev.) of 0.81, and a Predicted Residual Error Sum of Squares (PRESS) of 50.22. Statistical significance was observed for the linear terms (A, B, C, D), quadratic terms ($A^2$, $B^2$, $C^2$, $D^2$), and interaction terms (AB, BC, BD, and CD) at the $p < 0.05$ level; however, the AC and AD interactions were not statistically significant ($p > 0.05$).

Finally, the normality of the error distribution was confirmed by the uniform distribution of residuals in the normal probability plot (Fig. 7a). Additionally, the compact scatter of observed data points around the regression line in the predicted vs. actual plot (Fig. 7b) further validates the predictive accuracy of the model within the investigated design space.

**→ Table 3←**

**→ Fig. 7 ←**

### *3.6.2. Interaction effects of variables*

Three-dimensional response surface plots (Fig. 8) visualize interactions among the four independent variables and their cumulative effects on adsorption efficiency. These plots show the response surface curvature and help identify optimal operating conditions within the experimental design space.

- Effect of Initial Cd(II) concentration (A) and Nanocomposite dosage (B):

As shown in Fig. 8a, increasing the nanocomposite dosage from 20 to 40 mg initially enhances Cd(II) adsorption efficiency, likely because more active binding sites are available. At higher dosages, however, efficiency declines, possibly because particle aggregation or site saturation reduces the effective surface area. The selected range of Cd(II) concentration (40 to 80 mg $L^{-1}$) facilitates the establishment of adsorption isotherms and enables observation of equilibrium behavior without premature adsorbent saturation [43].

- Effect of Nanocomposite dosage (B) and Solution pH (C):

The interplay between dosage and solution pH is depicted in Fig. 8b. Solution pH is a critical determinant of adsorption. When the pH increases from 6 to 7, Cd(II) adsorption efficiency improves significantly, a typical pattern in metal-ion adsorption systems. At lower pH values, amine groups on the chitosan chains become protonated to $–NH_3^+$ and carboxyl groups remain protonated (–COOH), which may cause electrostatic repulsion toward the positively charged Cd(II) ions. As the pH increases, the surface sites undergo deprotonation and these groups are gradually converted to neutral $–NH_2$ and $–COO^-$, restoring the lone-pair electrons and increasing the negative surface charge. This strengthens electrostatic attraction and improves adsorption efficiency in the alkaline region, suggesting that the mechanism is primarily pH-dependent and governed by the adsorbent surface charge [44].

- Effect of Nanocomposite dosage (B) and Contact time (D):

The interaction between nanocomposite dosage and contact time in the range of 60 to 120 min is shown in Fig. 8c. Initially, the abundance of vacant active sites promotes rapid Cd(II) uptake. As contact time increases, the system approaches equilibrium, and the progressive occupation of active sites leads to a gradual deceleration in

the adsorption rate. So, extending the contact time beyond the equilibrium point yields only a minor improvement in adsorption efficiency.

- Effect of Solution pH (C) and Contact time (D):

Fig. 8d illustrates the interactive effect between solution pH and contact time. At lower pH levels, adsorption efficiency increases more slowly with time. This behavior suggests that competition between H+ ions and Cd(II) cations for active sites hinders rapid binding, necessitating a longer period to approach saturation. Conversely, at higher pH levels, the reduction in H+ concentration and the subsequent deprotonation of amine groups activate the surface sites. This promotes rapid cationic metal–ligand coordination, resulting in high adsorption efficiency in shorter contact times [45]. These findings demonstrate that Cd(II) adsorption is synergistically enhanced by optimized pH and contact time.

**→ Fig. 8←**

### *3.6.3. Optimization*

Following the evaluation of the operational variables influencing Cd(II) adsorption, the numerical optimization of the response surface model was performed to determine the optimal conditions for maximum removal efficiency (Fig. 9). The model predicted optimal operating parameters to be: an initial Cd(II) concentration of 68.62 mg $L^{-1}$, a nanocomposite dosage of 26.20 mg, a solution pH of 6.89, and a contact time of 79 min, providing the best balance between performance and operational economy. Under these optimized conditions, experimental validation was done in triplicate, yielding a mean adsorption efficiency of 91.60%. The close agreement (<0.05%) between the theoretical prediction (91.98%) and experimental results confirms the robustness, accuracy, and reliability of the developed quadratic model in describing the Cd(II) adsorption process.

**→ Fig. 9←**

### *3.6.4. Adsorption Kinetics and Isotherm Analysis*

A synergistic interplay at the molecular, thermodynamic, and kinetic levels governs the adsorption performance of the cold plasma–engineered CNPs/$TiO_2$/CuO/Chitosan nanocomposite. At the molecular interface, a high density of functional groups derived from activated CNPs and $TiO_2$/CuO, coupled with chitosan's $–NH_2$ and –OH, creates a heterogeneous binding environment. This environment facilitates rapid diffusion of metal ions to active sites. It promotes the formation of mixed-ligand complexes, which are thermodynamically more stable than those typically found in single-functional adsorbent systems [13]. Kinetic analysis revealed that the pseudo-second-order model best describes the adsorption process (Table 4), indicating that chemisorption is the rate-limiting step. The high correlation coefficient ($R^2$ = 0.9981) suggests that this step involves electron sharing

between the adsorbent surface and the Cd(II) ions. A maximum adsorption capacity (qe) of 120.45 mg $g^{-1}$ reflects the high affinity of metal ions for nitrogen-based donor atoms via coordinate covalent bonding, while simultaneously interacting with oxygenated functional groups to form stable chelate complexes.

**→ Table 4←**

Langmuir and Freundlich isotherm models were used to evaluate adsorption equilibrium behavior. Experimental data (qe versus Ce) were subjected to linear regression analysis to identify the most appropriate theoretical framework. As illustrated in Fig. 10a and 10b, the Freundlich isotherm showed a better fit to the experimental data, yielding a high $R^2$ of 0.9944 and a Freundlich constant ($n > 1$) indicating favorable adsorption conditions, as detailed in Table 5. It suggests adsorption on a heterogeneous surface, consistent with the cold plasma–engineered CNPs/$TiO_2$/CuO/Chitosan nanocomposite. This heterogeneity, together with the pseudo-second-order kinetic behavior, supports multi-site chemisorption involving complexation interactions between the Cd(II) ions and the diverse functional groups on the adsorbent surface.

**→ Fig. 10←**

**→ Table 5←**

***3.6.5. Comparative study***

Beyond environmental and economic considerations, an effective nanocomposite for heavy metal remediation must demonstrate a synergy between high adsorption capacity and rapid kinetics. This dual functionality is critical for minimizing reactor volumes and reducing both capital and operational expenditures. Table 6 presents a comparative study of adsorption performance across various nanocomposites reported in recent literature; however, direct comparisons are often complicated by disparate experimental protocols, including variations in pollutant concentration, nanocomposite dosage, synthesis methods, pH, and contact time. Furthermore, some nanocomposites achieve acceptable removal efficiencies only after prolonged reaction times or under strongly alkaline pH. The cold plasma–engineered CNPs/$TiO_2$/CuO/Chitosan nanocomposite exhibits an optimal balance of high efficacy and favorable kinetics, highlighting it as a candidate for advanced wastewater treatment applications.

**→ Table 6←**

***3.6.6. Adsorption mechanism***

The theoretical framework for heavy metal adsorption onto functionalized nanocomposites encompasses several mechanistic pathways, including electrostatic interactions, surface complexation, and coordinative bonding. In this study, the adsorption of Cd(II) onto the cold plasma–engineered CNPs/$TiO_2$/CuO/Chitosan nanocomposite is driven by the synergy between the plasma-activated CNPs and the ternary $TiO_2$/CuO/Chitosan framework (Fig. 10c). The cold plasma surface engineering yields enhanced complementary binding mechanisms unavailable in single-functional modification strategies. It creates a heterogeneous binding environment for Cd(II)'s distinct coordination preferences. This covalent attachment strategy ensures a robust linkage between the organic functional groups and the nanocomposite core, providing excellent chemical stability across a wide pH range. They exhibit amphoteric behavior, acting as both proton donors and acceptors depending on the solution pH. The chitosan coating has abundant amino and hydroxyl groups serving as reactive centers for chemical modification and Cd(II) sequestration. This inherent surface reactivity facilitates direct interaction with Cd(II) through electrostatic attraction and surface complexation. Recent investigations suggest that synergistic effects among functional groups enhance adsorption performance through cooperative binding mechanisms, in which one group facilitates the approach of metal ions while another provides additional stabilization via secondary interactions [52]. Furthermore, pH-dependent speciation of both functional groups and metal ions is critical; for instance, surface-bound moieties such as amino groups undergo protonation in acidic media, while carboxyl groups deprotonate under alkaline conditions, significantly modulating their respective binding capacities [53].

Under optimized conditions, the influence of temperature on Cd(II) adsorption (25°C to 70°C) was assessed (Fig. 10d). The results indicate that increasing temperature significantly enhances adsorption capacity, approaching near-complete removal at 70°C. This enhancement can be attributed to several factors: first, the reduced viscosity of the aqueous medium at elevated temperatures facilitates the diffusion of Cd(II) ions through the boundary layer surrounding the nanocomposite particles. Second, increased thermal energy enhances Cd(II) mobility, enabling deeper penetration into chitosan's internal porous architecture to access sequestered amino and hydroxyl sites [54]. Simultaneously, the inorganic $TiO_2$/CuO components provide essential thermal and mechanical stability, reinforcing the chitosan framework and preventing structural degradation under elevated thermal conditions. The positive correlation between temperature and removal efficiency confirms that the adsorption process is endothermic, suggesting that Cd(II) uptake is governed by chemisorption, which requires overcoming a specific activation energy barrier, rather than being driven solely by physisorption.

### *3.6.7. Selectivity*

The selectivity of the cold plasma–engineered CNPs/$TiO_2$/CuO/Chitosan nanocomposite was evaluated in binary systems with competing Pb(II) ions and multi-component matrices similar to real wastewater. In complex industrial streams, such as battery manufacturing effluents, cadmium and lead often coexist with other transition

metals. The adsorbent's surface affinity is governed by ionic physicochemical properties, including ionic radius, electronegativity, hydration energy, and coordination-geometry preferences, which determine selective uptake [55]. Cd(II) and Pb(II) behave differently in aquatic systems. Pb(II) ions predominantly undergo hydrolysis to species like $PbOH^+$ and $Pb(OH)_2$ above pH 6.0, while Cd(II) ions maintain a more stable divalent state across a broader pH range [56, 57].

Cd(II) ions exhibit intermediate behavior with a moderate preference for hard and soft donors, whereas Pb(II) ions show a pronounced affinity for sulfur- and nitrogen-based ligands [58]. Structural analysis suggests that optimal performance requires a precise balance of functional groups and spatial distribution. Theoretical modeling indicates that while high amino content enhances Pb(II) selectivity, it can impede overall capacity due to steric crowding; conversely, excessive oxygen-containing functional groups, such as carboxyl, promote nonspecific electrostatic interactions that diminish selectivity. In multi-metal systems, these interactions act synergistically due to surface-bridge formation, charge neutralization, or allosteric modulation, or antagonistically due to site competition and electrostatic repulsion [59]. In the Cd(II)– Pb(II) binary system, these behaviors are concentration-dependent. Synergistic effects often dominate at low concentrations, where heterogeneous binding sites remain available, while competitive inhibition prevails as concentrations increase [60].

Experimental results confirmed a marked selectivity for Cd(II) over Pb(II). In single-component systems, the equilibrium adsorption capacities (qe) reached 120.45 mg $g^{-1}$ for Cd(II) and 99.75 mg $g^{-1}$ for Pb(II) under the optimized conditions (solution containing 69 mg $L^{-1}$ of each metal ion, adsorbent dosage 26 mg, pH 6.9, contact time 79 min, and temperature 25°C). In binary systems, these capacities decreased to 85.65 mg $g^{-1}$ and 50.35 mg $g^{-1}$, respectively, confirming significant competitive adsorption. The selectivity coefficient values (αCd/Pb), ranging from 2.75 to 4.58, reached a maximum at pH 6.5 (Fig. 11a). This performance is attributed to the nanocomposite's engineered oxygen-donor-rich coordination environment, which, combined with the smaller ionic radius of Cd(II) (1.09 Å) relative to Pb(II) (1.32 Å), facilitates preferential mixed-ligand chelate formation [61].

Practical water treatment requires adsorbents that function effectively in complex aqueous environments. To evaluate the practical applicability of the cold plasma–engineered CNPs/$TiO_2$/CuO/Chitosan nanocomposite, interference studies were conducted with common environmental cations at a concentration of 100 mg $L^{-1}$ and pH 6.5 (Table 7). The results show that monovalent cations ($Na^+$, $K^+$), even at elevated concentrations (up to 10 times the concentration), cause minimal interference (< 5% reduction in Cd(II) and Pb(II) uptake). This tolerance is attributed to the negligible affinity of these hard, non-coordinating ions for the target functional groups. By contrast, divalent cations ($Ca^{2+}$, $Mg^{2+}$, $Zn^{2+}$, and $Ni^{2+}$) exhibit moderate competitive effects, causing a 10-15% decrease in Cd(II) and a 15-20% decrease in Pb(II) adsorption capacities. The selectivity of the adsorbent was further evaluated in competitive multi-metal systems (mixed ions). Fig. 11b compares the αCd/Pb value in binary

systems with those in the presence of interfering ions. Despite the competitive decline, the αCd/Pb remained above 2.75, validating the proposed coordination-based binding mechanism and confirming the efficacy of the multi-functional surface modification [62].

**→ Fig. 11←**

**→ Table 7←**

***3.6.8. Reusability study***

To assess the economic viability of the cold plasma–engineered CNPs/$TiO_2$/CuO/Chitosan nanocomposite, its reusability and stability were evaluated over five consecutive adsorption-desorption cycles. Desorption was driven by protonation of surface-active sites and release of bound metal ions through competitive ligand exchange [63]. HCl (1 M) showed the highest Cd(II) desorption efficiency (> 92%) within 60 min among the desorbing agents $HNO_3$, EDTA, and $Na_2CO_3$. After acidic desorption, the nanocomposite was centrifuged, washed with an ethanol/DI water mixture, and dried at 40°C for 24 h before reuse. As shown in Fig. 11c, after five cycles, Cd(II) adsorption efficiency decreased from 91.98% to 87.25%, and the maximum adsorption capacity (qe) declined from 120.45 mg $g^{-1}$ to 104.75 mg $g^{-1}$. This reduction likely reflects incomplete metal desorption, accumulation of irreversibly bound species at high-affinity sites, partial site blocking, or minor nanoparticle loss during regeneration. Nevertheless, the adsorbent maintained robust performance across all cycles. Post-recycling FTIR analysis (Fig. 11d) revealed minimal changes in the characteristic functional group bands, confirming the chemical stability and structural integrity of the nanocomposite.

## 4. Conclusions

This work reports the synthesis and characterization of a novel cold plasma–engineered CNPs/$TiO_2$/CuO/Chitosan nanocomposite, offering a highly efficient and sustainable material for Cd(II) sequestration from aqueous media. Through green cold-plasma surface engineering, a chemically heterogeneous surface with enhanced functional group density was achieved. This synergistic modification, integrated with the structural stability and abundant active sites of the ternary $TiO_2$/CuO/Chitosan matrix, facilitated superior adsorption performance and effectively bypassed the limitations inherent in single-functional surface modifications. Optimization via response surface methodology (RSM) identified pH, dosage, and contact time as critical parameters. Under optimized conditions (pH 6.89, 26.20 mg/50 mL, and 79 min), the nanocomposite achieved a peak Cd(II) removal efficiency of 91.98% with an equilibrium capacity of 120.45 mg $g^{-1}$, even at a high initial Cd(II) concentration of 68.62 mg $L^{-1}$. Kinetic and isotherm modeling confirmed a chemisorption-dominated mechanism, following pseudo-second-order kinetics and Freundlich multilayer adsorption.

Furthermore, competitive studies revealed high selectivity for Cd(II) over Pb(II) ($\alpha Cd/Pb = 4.58$ at pH 6.5). The nanocomposite also demonstrated excellent reusability, maintaining 87.25% efficiency over five cycles, underscoring its economic viability and potential for advanced wastewater treatment.

**CRediT authorship contribution statement**

Mehrnaz Akhundi Nematzadeh: Software, Data curation, Analysis, Methodology, Writing-original draft, and Investigation. Sahar Baniyaghoob: Conceptualization, Writing-review & editing, Supervision, Software, Investigation, Project administration, Methodology, Validation, and Data curation. Shahrooz Saviz: Software, Investigation, Analysis, and Data curation. Reza Fazaeli: Software, Investigation, Methodology, and Resources. All authors have read and approved the final manuscript.

**Conflicts of interest**

The authors declare that they have no conflicts of interest. Furthermore, no other individuals meet the criteria for authorship. Dr. Sahar Baniyaghoob is the designated Corresponding Author and sole point of contact throughout the editorial process, managing all communications regarding manuscript progress, revisions, and final proof approvals with the editorial office and other authors. The Corresponding Author's email address is confirmed to be current and accurate.

**Acknowledgments**

The authors gratefully acknowledge the Department of Chemistry at the Science and Research Branch (SR.C.) of the Islamic Azad University for their support of this research.

**Funding**

This research did not receive any specific grant from funding agencies in the public, commercial, or not-for-profit sectors.

**Compliance with ethical standards**

Ethical approval does not apply to this article.

**Data availability**

All data supporting the findings of this study were collected in the chemistry lab of the Islamic Azad University. These data have not been published previously and are available upon request from the Corresponding Author. All sources have been properly cited in the Reference section.

**Consent for publication**

All authors grant their permission for submission and publication of this manuscript.

**References**


[1] V. Singh, N. Singh, S.N. Rai, A. Kumar, A.K. Singh, M.P. Singh, V. Mishra, Heavy metal contamination in the aquatic ecosystem: toxicity and its remediation using eco-friendly approaches, *Toxics*, 11 (2023), 147. https://doi.org/10.3390/toxics11020147.

[2] A. Mandal, P.S. Kumar, C.S. Poorva, L.S. Raju, S.R. Balasubramani, Research progress of persistent organic pollutants in water: classification, sources, potential risks, and treatment approaches, *Water Pract.*, 19 (2024), 937-959. https://doi.org/10.2166/wpt.2024.031.

[3] P.K. Singh, U. Kumar, I. Kumar, A. Dwivedi, P. Singh, S. Mishra, R.K. Sharma, Critical review on toxic contaminants in surface water ecosystem: sources, monitoring, and its impact on human health, *Environ. Sci. Pollut. Res.*, 31 (2024), 56428-56462. https://doi.org/10.1007/s11356-024-34932-0.

[4] J. Briffa, E. Sinagra, R. Blundell, Heavy metal pollution in the environment and their toxicological effects on humans, *Heliyon*, 6 (2020), e04691. https://doi.org/10.1016/j.heliyon.2020.e04691.

[5] Y. Yan, L. Jin, J. Li, G. Chen, Association of cadmium and lead exposure with mortality in cancer survivors: a prospective cohort study, *Ecotoxicol. Environ. Saf.*, 292 (2025), 117960. https://doi.org/10.1016/j.ecoenv.2025.117960.

[6] S. Kotnala, S. Tiwari, A. Nayak, B. Bhushan, S. Chandra, C.R. Medeiros, H.D.M. Coutinho, Impact of heavy metal toxicity on the human health and environment, *Sci. Total Environ.*, 987 (2025), 179785. https://doi.org/10.1016/j.scitotenv.2025.179785.

[7] R. Chakraborty, A. Asthana, A.K. Singh, B. Jain, A.B.H. Susan, Adsorption of heavy metal ions by various low-cost adsorbents: a review, *Int. J. Environ. Anal. Chem.*, 102 (2022), 342-379. https://doi.org/10.1080/03067319.2020.1722811.

[8] D.B. Olawade, O.Z. Wada, B.I. Egbewole, O. Fapohunda, A.O. Ige, S.O. Usman, O. Ajisafe, Metal and metal oxide nanomaterials for heavy metal remediation: novel approaches for selective, regenerative, and scalable water treatment, *Front. Nanotechnol.*, 6 (2024), 1466721. https://doi.org/10.3389/fnano.2024.1466721.

[9] H. Rafeeq, A. Hussain, A. Ambreen, M. Waqas, M. Bilal, H.M. Iqbal, Functionalized nanoparticles and their environmental remediation potential: a review, *J. Nanostruct. Chem.*, 12 (2022), 1007-1031. https://doi.org/10.1007/s40097-021-00468-9.

[10] V.P. Kothavale, A. Sharma, R.P. Dhavale, V.D. Chavan, S.R. Shingte, O. Selyshchev, P.B. Patil, Carboxyl and thiol-functionalized magnetic nano-adsorbents for efficient and simultaneous removal of Pb (II), Cd (II), and Ni (II) heavy metal ions from aqueous solutions: Studies of adsorption, kinetics, and isotherms, *J. Phys. Chem. Solids*, 172 (2023), 111089. https://doi.org/10.1016/j.jpcs.2022.111089.

[11] U.N. Danmallam, A.A. Adeleke, Z.U. Zango, Adsorptive removal of phenanthrene and naphthalene from wastewater using coal derived carbon nanoparticles with kinetic and thermodynamic evaluation, *Sci. Rep.,* 15 (2025), 39118. https://doi.org/10.1038/s41598-025-27116-4.

[12] S. Rezania, N. Darajeh, P.F. Rupani, A. Mojiri, H. Kamyab, M. Taghavijeloudar, Recent advances in the adsorption of different pollutants from wastewater using carbon-based and metal-oxide nanoparticles, *Appl. Sci.*, 14 (2024), 11492. https://doi.org/10.3390/app142411492.

[13] M. Yang, S. Dang, L. Gao, J. Zhang, Dual-functional amino-carboxyl co-modified $Fe_3O_4$ nanoparticles for synergistic selective adsorption of lead and cadmium ions from aqueous solutions, *Sci. Rep*., 16 (2026), 7676. https://doi.org/10.1038/s41598-026-38809-9.

[14] M. Wołowiec, M. Komorowska-Kaufman, A. Pruss, G. Rzepa, T. Bajda, Removal of heavy metals and metalloids from water using drinking water treatment residuals as adsorbents: A review, *Miner.*, 9 (2019), 487. https://doi.org/10.3390/min9080487.

[15] Y. Liang, L. Zheng, Y. Yang, X. Zheng, D. Xiao, B. Ai, Z. Sheng, Dielectric barrier discharge cold plasma modifies the multiscale structure and functional properties of banana starch, *Int. J. Biol. Macromol.*, 264 (2024), 130462. https://doi.org/10.1016/j.ijbiomac.2024.130462.

[16] S. Deng, N. Takeuchi, T. Kaneko, Atmospheric Pressure Plasma for Carbon Material Modification and Synthesis: A Comprehensive Review, *Mater.*, 18 (2024), 5662. https://doi.org/10.3390/ma18245662.

[17] X. Wang, J. Wang, Z. Wang, W. Yan, H. Zhuang, J. Zhang, Impact of dielectric barrier discharge cold plasma on the lipid oxidation, color stability, and protein structures of myoglobin-added washed pork muscle, *Front. Nutr.*, 10 (2023), 1137457. https://doi.org/10.3389/fnut.2023.1137457.

[18] H. Jiao, R. Bi, A. Xu, G. Zhang, L. Zhai, H. Dong, L. Hu, C. Dai, B. Li, Z. Wang, Efficient adsorption and advanced purification of metal ions induced by synergistic effect of amine and thione on covalent organic frameworks, *Colloids Surf. A: Physicochem. Eng. Asp.*, 691 (2024), 133924. https://doi.org/10.1016/j.colsurfa.2024.133924.

[19] T.P. Fato, D.W. Li, L.J. Zhao, K. Qiu, Y.T. Long, Simultaneous removal of multiple heavy metal ions from river water using ultrafine mesoporous magnetite nanoparticles. *ACS Omega*, 4 (2019), 7543-7549. https://doi.org/10.1021/acsomega.9b00731.

[20] A.F.P. Allwin Mabes Raj, M. Bauman, M. Lakić, N. Dimitrušev, A. Lobnik, A. Košak, Removal of $Pb^{2+}$, Cr, and $Hg^{2+}$ ions from aqueous solutions using amino-functionalized magnetic nanoparticles, *Int. J. Mol. Sci.*, 23 (2022), 16186. https://doi.org/10.3390/ijms232416186.

[21] H.G. Palhares, P.H. Andrade, A. Moissette, C. Volkringer, T. Loiseau, M. Houmard, E.H. Nunes, Simultaneous adsorption of anionic and cationic species on UiO-66 and MIL-125 MOFs: Mechanisms & selectivity, *Microporous Mesoporous Mater.*, 368 (2024), 113010. https://doi.org/10.1016/j.micromeso.2024.113010.

[22] P. Cheng, T. Chen, T. Liu, Y. Wei, M. Tian, X. Cao, J. Zhu, Covalent/metal–organic framework membranes with tailored pore functionality for accurate ion separation, *Chem. Sci.*, 16 (2025), 22900-22932. https://doi.org/10.1039/d5sc07238g.

[23] Q. Qu, L. Qiu, M.Z. Li, G.T. Sun, H.Y. Chen, X.H. Guo, Synergistic effects of pyrolysis temperature, iron ion concentration and solid/liquid ratio on the properties and Cr (VI) removal performance of magnetic carbon, *J. Water Process Eng.*, 53 (2023), 103785. https://doi.org/10.1016/j.jwpe.2023.103785.

[24] I.O. Saheed, W. Da Oh, F.B.M. Suah, Chitosan modifications for adsorption of pollutants–A review, *J. Hazard. Mater.*, 408 (2021), 124889. https://doi.org/10.1016/j.jhazmat.2020.124889.

[25] Y. Yu, Y. Peng, Y. Zhong, Z. Su, S. Vijayakumar, Y. Chen, Y. Mao, L. Wang, M. Xin, M. Li, Innovative pH-responsive chitosan hydrogel: A systematic study on VB12 controlled release and multifunctional biological effects via synergistic grafting of cysteine and arginine, *Int. J. Biol. Macromol.*, 322 (2025), 146718. https://doi.org/10.1016/j.ijbiomac.2025.146718.

[26] K.Y. Kumar, H.B. Muralidhara, Y.A. Nayaka, J. Balasubramanyam, H. Hanumanthappa, Low-cost synthesis of metal oxide nanoparticles and their application in adsorption of commercial dye and heavy metal ion in aqueous solution, *Powder Technol.*, 246 (2013), 125-136. https://doi.org/10.1016/j.powtec.2013.05.017.

[27] A.A. Mashentseva, N. Seitzhapar, M. Barsbay, N.A. Aimanova, A.N. Alimkhanova, D.A. Zheltov, D.T. Sadyrbekov, Adsorption isotherms and kinetics for Pb (ii) ion removal from aqueous solutions with biogenic metal oxide nanoparticles, *RSC Adv.*, 13 (2023), 26839-26850. https://doi.org/10.1039/d3ra05347d.

[28] L. Ma, J. Zheng, F. Li, Y. Chen, R. He, J. Zhang, N. Wang, Z. Ning, Z. Zhao, Valence-Dependent Adsorption of Sb(III) and Sb(V) on Spinel $MFe_2O_4$ Ferrites: Spectroscopic Insights into Surface Hydroxyl and Metal–Oxygen Interactions, *Water*, 18 (2026), 569. https://doi.org/10.3390/w18050569.

[29] A. Kovács, Z. Varga, Theoretical Study of Metal–Ligand Interactions in Lead Complexes with Radiopharmaceutical Interest, *Molecules*, 29 (2024), 4198. https://doi.org/10.3390/molecules29174198.

[30] A.E. Mubark, S.M. El-Gamasy, A.M. Masoud, A.A. El-Zahhar, M.M. Alghamdi, M.H. Taha, T.F. Hassanein, Efficient Schiff base ligand for selective Cd (ii) and Pb (ii) removal from water, *RSC Adv.*, 15 (2025), 21987. https://doi.org/10.1039/d5ra03053f.

[31] K. Yang, B. Chen, X. Zhu, B. Xing, Aggregation, adsorption, and morphological transformation of graphene oxide in aqueous solutions containing different metal cations, *Environ. Sci. Technol.*, 50 (2016), 11066-11075. https://doi.org/10.1021/acs.est.6b04235.

[32] B.T. Danat, R.A. Wuana, H.F. Chahul, Review of adsorption isotherms models, *Appl. Water Sci.,* 16 (2026), 72. https://doi.org/10.1007/s13201-025-02682-0.

[33] Z. Sun, C. Tian, T. Yang, J. Fu, H. Xu, Y. Wang, Z. Lin, A MOF-based trap with strong affinity toward low-concentration heavy metal ions, *Sep. Purif. Technol.*, 301 (2022), 121946. https://doi.org/10.1016/j.seppur.2022.121946.

[34] M.J. Kadhim, F. Allawi, M.A. Mahdi, S.N. Abaas, High Photocatalytic Performance of Zno/$Fe_3O_4$ and $TiO_2$/$Fe_3O_4$ Nanostructures Thin Films against Methylene Blue Dye under Visible Light Irradiation, *Iran. J. Mater. Sci. Eng.,* 19 (2022). https://doi.org/10.22068/ijmse.2461.

[35] A. Benettayeb, F.Z. Seihoub, P. Pal, S. Ghosh, M. Usman, C.H. Chia, M. Sillanpää, Chitosan nanoparticles as potential nano-sorbent for removal of toxic environmental pollutants, *Nanomater.*, 13 (2023), 447. https://doi.org/10.3390/nano13030447.

[36] A. Jiang, X. Huang, G. Zhang, W. Yang, A study of the degradation of LEV by transparent PVA/NCD-$TiO_2$ nanocomposite films with enhanced visible-light photocatalytic activity, *Catal.*, 12 (2022), 1336. https://doi.org/10.3390/catal12111336.

[37] N. Esfandiar, R. Suri, E.R. McKenzie, Competitive sorption of Cd, Cr, Cu, Ni, Pb and Zn from stormwater runoff by five low-cost sorbents; Effects of co-contaminants, humic acid, salinity and pH, *J. Hazard. Mater.*, 423 (2022), 126938. https://doi.org/10.1016/j.jhazmat.2021.126938.

[38] A. Dambuza, P.P. Mokolokolo, M.E. Makhatha, M.A. Sibeko, Chitosan-based materials as effective materials to remove pollutants, *Polym.*, 17 (2025), 2447. https://doi.org/10.3390/polym17182447.

[39] E. Ahangaran, H. Aghaie, R. Fazaeli, Adsorption study of Ni (II) ion and azo dye DR278 in aqueous media using $MoS_2$/OMWCNTs adsorbent and optimization by response surface methodology, *J. Nanoanal*., 10, 560-577.

[40] N.E. Fard, R. Fazaeli, R. Ghiasi, Band Gap Energies and Photocatalytic Properties of CdS and Ag/CdS Nanoparticles for Azo Dye Degradation, *Chem. Eng. Technol*., 39 (2016) 149-157. https://doi.org/10.1002/ceat.201500116.

[41] Y. Ding, S. Maitra, C. Wang, R. Zheng, T. Barakat, S. Roy, B.L. Su, Bi-functional Cu-$TiO_2$/CuO photocatalyst for large-scale synergistic treatment of waste sewage containing organics and heavy metal ions, *Sci. China Mater.*, 66 (2023), 179-192. https://doi.org/10.1007/s40843-022-2148-4.

[42] V. Rangel-Contreras, O. Reyes-Vallejo, V. Subramaniam, Synthesis of $TiO_2$/CuO/GO nanocomposite for the photocatalytic degradation of methylene blue, *J. Mater. Sci.: Mater. Electron.*, 35 (2024), 1301. https://doi.org/10.1007/s10854-024-12986-7.

[43] G. Lemessa, Y. Chebude, A.G. Demesa, E. Fadeev, T. Koiranen, E. Alemayehu, Development of suitable magnetite–diatomite nanocomposite for Cd (II) adsorptive removal from wastewater, *Sci. Afr.*, 24 (2024), e02213. https://doi.org/10.1016/j.sciaf.2024.e02213.

[44] A. Mohammed Ahmed, M. Leul Mekonnen, K. Nigussie Mekonnen, Polymer-based nanocomposite adsorbents for resource recovery from wastewater, *RSC Adv.* 13 (2023), 31687–31703. https://doi.org/10.1039/d3ra05453e.

[45] G. Wu, J. Ma, S. Li, S. Wang, B. Jiang, S. Luo, J. Li, X. Wang, Y. Guan, L. Chen, Cationic metal-organic frameworks as an efficient adsorbent for the removal of 2,4-dichlorophenoxyacetic acid from aqueous solutions, *Environ. Res.*, 186 (2020), 109542. https://doi.org/10.1016/j.envres.2020.109542.

[46] M. Kavisri, M. Abraham, S.K.R. Namasivayam, J. Aravindkumar, D. Balaji, R. Sathishkumar, M. Moovendhan, Adsorption isotherm, kinetics and response surface methodology optimization of cadmium (Cd) removal from aqueous solution by chitosan biopolymers from cephalopod waste, *J. Environ. Manag.*, 335 (2023), 117484. https://doi.org/10.1016/j.jenvman.2023.117484.

[47] A.F. Abdel-Magied, R.M. Ashour, L. Fu, M. Dowaidar, W. Xia, K. Forsberg, H.N. Abdelhamid, Magnetic metal-organic frameworks for efficient removal of cadmium (II), and lead (II) from aqueous solution, *J. Environ. Chem. Eng.*, 10 (2022). https://doi.org/10.1016/j.jece.2022.107467.

[48] H. Fu, H. He, R. Zhu, L. Ling, W. Zhang, Q. Chen, Phosphate modified magnetite@ ferrihydrite as a magnetic adsorbent for Cd (II) removal from water, soil, and sediment, *Sci. Total Environ.*, 764 (2021), 142846. https://doi.org/10.1016/j.scitotenv.2020.142846.

[49] Y. Wang, Y. Liu, T. Chao, Q. Li, Y. Wang, Q. Zhao, Y. Wang, High efficiency adsorption of Cd (II) by $KHCO_3$-activated Fe/Mn co-modified peanut shell biochar: adsorption performance, mechanisms, and life cycle assessment, *Chem. Eng. Sci.*, (2025) 122747. https://doi.org/10.1016/j.ces.2025.122747.

[50] J. Lin, B. Su, M. Sun, B. Chen, Z. Chen, Biosynthesized iron oxide nanoparticles used for optimized removal of cadmium with response surface methodology, *Sci. Total Environ.*, 627 (2018), 314-321. https://doi.org/10.1016/j.scitotenv.2018.01.170.

[51] M.A. Salam, G. Al-Zhrani, S.A. Kosa, Simultaneous removal of copper (II), lead (II), zinc (II) and cadmium (II) from aqueous solutions by multi-walled carbon nanotubes, *Comptes rendus chimie*, 15 (2012), 398-408. https://doi.org/10.1016/j.crci.2012.01.013.

[52] E.R. Tarigan, E. Frida, S. Humaidi, S. Susilawati, Adsorption mechanism of heavy metals using activated carbon derived from hydrilla verticillata, *Trends Sci.*, 22 (2025), 8732-8732. https://doi.org/10.48048/tis.2025.8732.

[53] M. Gorohovs, Y. Dekhtyar, Surface Functionalization of Nanoparticles for Enhanced Electrostatic Adsorption of Biomolecules, *Molecules*, 30 (2025), 3206. https://doi.org/10.3390/molecules30153206.

[54] Y. Yu, W. Liu, Y. Zhang, B. Zhang, Y. Jin, S. Chen, G. Chen, Chitosan/magnetic biochar composite with enhanced reusability: Synergistic effect of functional groups and multilayer structure, *Arab. J. Chem.*, 17 (2024), 105746. https://doi.org/10.1016/j.arabjc.2024.105746.

[55] Z. Wang, W. Xu, F. Jie, The selective adsorption performance and mechanism of multiwall magnetic carbon nanotubes for heavy metals in wastewater, *Sci. Rep.,* 11 (2021), 16878. https://doi.org/10.1038/s41598-021-96465-7.

[56] X. Zeng, G. Zhang, J. Zhu, Selective adsorption of heavy metals from water by a hyper-branched magnetic composite material: Characterization, performance, and mechanism, *J. Environ. Manag.*, 314 (2022), 114979. https://doi.org/10.1016/j.jenvman.2022.114979.

[57] R. Chen, C. Gan, B. Cai, R. Liu, W. Xu, W. Yin, H. Li, L. Yu, Q. Yong, Co-adsorption and selective-adsorption of heavy metals and dyes from aqueous solution by bio-based humus/chitosan hydrogels, *J. Environ. Sci.*, 145 (2024), 193-204. https://doi.org/10.1016/j.jes.2023.09.004.

[58] C. Bulin, R. Zheng, T. Guo, B. Zhang, Incorporating hard-soft acid-base theory in multi-aspect analysis of the adsorption mechanism of aqueous heavy metals by graphene oxide, *J. Phys. Chem. Solids*, 170 (2022), 110934. https://doi.org/10.1016/j.jpcs.2022.110934.

[59] A.A. Markeb, J. Moral-Vico, A. Sanchez, X. Font, Optimization of lead (II) removal from water and wastewater using a novel magnetic nanocomposite of aminopropyl triethoxysilane coated with carboxymethyl cellulose cross-linked with chitosan nanoparticles, *Arab. J. Chem.*, 16 (2023), 105022. https://doi.org/10.1016/j.arabjc.2023.105022.

[60] M.d. Rabiul Awual, M. Khraisheh, N.H. Alharthi, Efficient detection and adsorption of cadmium(II) ions using innovative nano-composite materials, *Chem. Eng. J.,* 343 (2018), 118-127. https://doi.org/10.1016/j.cej.2018.02.116.

[61] C.M. Simonescu, F. Dumitru, B. Zărnescu, D.C. Culiţă, A. Răzvan, O. Oprea, R. Truşcă, E. Vasile, Competitive Adsorption of Aqueous Cd(II) and Pb(II) Solutions onto Silicas Synthesized with Saponin as Template Agent, *J. Compos. Sci.*, 8 (2024), 227. https://doi.org/10.3390/jcs8060227.

[62] D. Siswanta, P.D. Ola, Adsorption Characteristics of Pb (II) and Cd (II) Ions on Dithizone-loaded Natural Zeolite, *J. Ion Exchange*, 18 (2007), 564-569. https://doi.org/10.5182/jaie.18.564.

[63] D.A. Gkika, A.K. Tolkou, I.A. Katsoyiannis, G.Z. Kyzas, The adsorption-desorption-regeneration pathway to a circular economy: the role of waste-derived adsorbents on chromium removal, *Sep. Purif. Technol.*, 368 (2025), 132996. https://doi.org/10.1016/j.seppur.2025.132996.

**Figure Captions**

**Fig. 1.** Schematic illustration of the preparation procedure of the cold plasma–engineered CNPs/$TiO_2$/CuO/Chitosan nanocomposite.

**Fig. 2.** XRD patterns of the cold plasma–engineered CNPs and the cold plasma–engineered CNPs/$TiO_2$/CuO/Chitosan nanocomposite.

**Fig. 3.** FT-IR spectra of the cold plasma–engineered CNPs and the cold plasma–engineered CNPs/$TiO_2$/CuO/Chitosan nanocomposite.

**Fig. 4.** (a) EDX spectrum and (b) XPS survey scan spectrum of the cold plasma–engineered CNPs/$TiO_2$/CuO/Chitosan nanocomposite with its fitted spectra of (c) C 1s, (d) Ti 2p, (e) O 1s, and (f) Cu 2p.

**Fig. 5.** (a) $N_2$ adsorption-desorption isotherms and (b) BJH pore size distribution plots of the cold plasma–engineered CNPs and the cold plasma–engineered CNPs/$TiO_2$/CuO/Chitosan nanocomposite. (c) Zeta potential of the cold plasma–engineered CNPs/$TiO_2$/CuO/Chitosan nanocomposite.

**Fig. 6.** (a-d) FESEM images and (e) Particle size distribution curve of the nanocomposite. (f-i) TEM images and (j) Particle size distribution curve of the nanocomposite.

**Fig. 7.** Model validation plots of (a) Normal probability vs. residuals, and (b) Predicted vs. actual values.

**Fig. 8.** Response surface plots (3D) for Cd(II) adsorption efficiency: (a) Effect of Initial Cd(II) concentration (A) and Nanocomposite dosage (B), (b) Effect of Nanocomposite dosage (B) and Solution pH (C), (c) Effect of Nanocomposite dosage (B) and Contact time (D), and (d) Effect of Solution pH (C) and Contact time (D).

**Fig. 9.** Desirability ramp for numerical optimization.

**Fig. 10.** Linear isotherm plots for Cd(II) adsorption: (a) Langmuir, and (b) Freundlich models. (c) Adsorption mechanism illustration, and (d) Influence of temperature on Cd(II) adsorption efficiency under optimized conditions.

**Fig. 11** (a) Selective adsorption coefficient of Cd(II) and Pb(II) under different pH conditions, and (b) Effect of interfering ions on the selectivity coefficient αCd/Pb. Reusability and stability evaluation: (c) Adsorption efficiency and capacity over five consecutive cycles, and (d) FTIR spectra comparison of the fresh and regenerated cold plasma–engineered CNPs/$TiO_2$/CuO/Chitosan nanocomposite.

**Table 1**

The five-level operating variables used for four independent parameters

| Factor | Name | Unit | Levels | | | | |
|---|---|---|---|---|---|---|---|
| | | | **-α** | **-1** | **0** | **+1** | **+α** |
| A | Initial Cd(II) concentration | mg $L^{-1}$ | 20 | 40 | 60 | 80 | 100 |
| B | Nanocomposite dosage | mg | 10 | 20 | 30 | 40 | 50 |
| C | Solution pH | --- | 5.5 | 6.0 | 6.5 | 7.0 | 7.5 |
| D | Contact time | min | 30 | 60 | 90 | 120 | 150 |

**Table 2**

The central composite design (CCD) model

| Run | A<br>Initial Cd(II) concentration | B<br>Nanocomposite dosage | C<br>Solution pH | D<br>Contact time | R1<br>Adsorption efficiency |
|---|---|---|---|---|---|
| | mg $L^{-1}$ | mg | | min | % |
| 1 | 40 | 20 | 7.0 | 60 | 83.42 |
| 2 | 40 | 40 | 6.0 | 60 | 78.86 |
| 3 | 40 | 20 | 6.0 | 120 | 76.78 |
| 4 | 100 | 30 | 6.5 | 90 | 94.17 |
| 5 | 80 | 20 | 6.0 | 60 | 68.02 |
| 6 | 80 | 40 | 7.0 | 60 | 96.48 |
| 7 | 60 | 30 | 6.5 | 90 | 88.29 |
| 8 | 80 | 40 | 7.0 | 120 | 89.37 |
| 9 | 40 | 40 | 7.0 | 120 | 77.26 |
| 10 | 80 | 20 | 6.0 | 120 | 83.98 |
| 11 | 40 | 20 | 6.0 | 60 | 62.16 |
| 12 | 60 | 30 | 6.5 | 90 | 87.57 |
| 13 | 60 | 50 | 6.5 | 90 | 67.47 |
| 14 | 60 | 30 | 6.5 | 90 | 88.89 |
| 15 | 80 | 20 | 7.0 | 120 | 90.48 |
| 16 | 40 | 20 | 7.0 | 120 | 83.59 |
| 17 | 60 | 30 | 6.5 | 150 | 96.45 |
| 18 | 20 | 30 | 6.5 | 90 | 77.37 |
| 19 | 80 | 40 | 6.0 | 60 | 90.48 |
| 20 | 40 | 40 | 7.0 | 60 | 86.40 |
| 21 | 80 | 20 | 7.0 | 60 | 88.26 |
| 22 | 60 | 30 | 6.5 | 90 | 88.86 |
| 23 | 40 | 40 | 6.0 | 120 | 84.51 |
| 24 | 60 | 30 | 7.5 | 90 | 99.99 |
| 25 | 60 | 30 | 5.5 | 90 | 89.37 |
| 26 | 60 | 30 | 6.5 | 90 | 88.55 |
| 27 | 80 | 40 | 6.0 | 120 | 96.48 |
| 28 | 60 | 30 | 6.5 | 30 | 88.17 |
| 29 | 60 | 10 | 6.5 | 90 | 49.48 |
| 30 | 60 | 30 | 6.5 | 90 | 89.08 |

**Table 3**

ANOVA results for Cd(II) adsorption

| Source | Sum of squares | df | Mean square | F-value | p-value | |
|---|---|---|---|---|---|---|
| Model | 3486.63 | 14 | 249.04 | 378.93 | < 0.0001 | significant |
| A- Initial Cd(II) concentration | 452.14 | 1 | 452.14 | 687.95 | < 0.0001 | |
| B- Nanocomposite dosage | 409.45 | 1 | 409.45 | 622.99 | < 0.0001 | |
| C- Solution pH | 235.94 | 1 | 235.94 | 358.99 | < 0.0001 | |
| D- Contact time | 84.11 | 1 | 84.11 | 127.98 | < 0.0001 | |
| AB | 27.54 | 1 | 27.54 | 41.90 | < 0.0001 | |
| AC | 0.4658 | 1 | 0.4658 | 0.7087 | 0.4131 | |
| AD | 2.08 | 1 | 2.08 | 3.17 | 0.0955 | |
| BC | 193.42 | 1 | 193.42 | 294.29 | < 0.0001 | |
| BD | 88.22 | 1 | 88.22 | 134.23 | < 0.0001 | |
| CD | 196.63 | 1 | 196.63 | 299.18 | < 0.0001 | |
| $A^2$ | 8.97 | 1 | 8.97 | 13.65 | 0.0022 | |
| $B^2$ | 1500.26 | 1 | 1500.26 | 2282.68 | < 0.0001 | |
| $C^2$ | 75.29 | 1 | 75.29 | 114.55 | < 0.0001 | |
| $D^2$ | 30.99 | 1 | 30.99 | 47.16 | < 0.0001 | |
| Residual | 9.86 | 15 | 0.6572 | | | |
| Lack of Fit | 8.34 | 10 | 0.8338 | 2.74 | 0.1385 | not significant |
| Pure Error | 1.52 | 5 | 0.3040 | | | |
| Cor Total | 3496.49 | 29 | | | | |
| Std. Dev. | 0.8107 | | $R^2$ | 0.9972 | | |
| Mean | 84.34 | | Adjusted $R^2$ | 0.9945 | | |
| C.V. % | 0.9612 | | Predicted $R^2$ | 0.9856 | | |
| PRESS | 50.22 | | Adeq Precision | 88.5157 | | |

**Table 4**

The parameters of the pseudo-second-order kinetic model obtained for Cd(II) adsorption

| **Linear equation on the pseudo-second- order kinetics** | **$q_e$ mg $g^{-1}$** | **$K_2$ g $mg^{-1}$ $min^{-1}$** | **$R^2$** |
|---|---|---|---|
| Y= 0.274x + 5.581 | 120.45 | 0.0134 | 0.9981 |

**Table 5**

Isotherm parameters of Cd(II) adsorption

| Isotherm model | Parameter | Value |
|---|---|---|
| Langmuir | $K_L$ (L $mg^{-1}$) | 0.2028 |
| | $q_{max}$ (mg $g^{-1}$) | 34.965 |
| | $R^2$ | 0.9712 |
| Freundlich | $K_F$ (L $mg^{-1}$) | 6.3841 |
| | n | 1.0357 |
| | $R^2$ | 0.9944 |

**Table 6**

Comparative study for Cd(II) adsorption using various nanocomposites reported in the literature

| Nanocomposite | pH | Time (min) | Adsorption efficiency (%) | Ref. |
|---|---|---|---|---|
| Chitosan biopolymers from cephalopods | 7.0 | 220 | 32.00 | [46] |
| Magnetic metal-organic frameworks | 6.0 | 120 | 87.00 | [47] |
| Phosphate modified magnetite@ ferrihydrite | 6.0 | 50 | 80.00 | [48] |
| $KHCO_3$-activated Fe/Mn co-modified peanut shell biochar | 7.0 | 90 | 84.00 | [49] |
| Iron oxide nanoparticles | 8.1 | --- | 98.50 | [50] |
| Multi-walled carbon nanotubes | 7.0 | 120 | 31.44 | [51] |
| cold plasma–engineered CNPs/$TiO_2$/CuO/Chitosan | 6.9 | 79 | 91.98 | Current |

**Table 7**

Effect of interfering ions on the selectivity coefficient αCd/Pb. Initial Cd(II) and Pb(II) concentration, each 69 mg $L^{-1}$, adsorbent dosage 26 mg, pH 6.5, contact time 79 min, and temperature 25°C

| **Interfering ion** | **Concentration mg $L^{-1}$** | **$q_e$, Cd(II) mg $g^{-1}$** | **$q_e$, Pb(II) mg $g^{-1}$** | **Selectivity αCd/Pb** |
|---|---|---|---|---|
| None (control) | 0 | 85.65 | 50.35 | 4.58 |
| $Na^+$ | 1000 | 85.28 | 48.85 | 4.47 |
| $K^+$ | 1000 | 85.16 | 48.73 | 4.45 |
| $Ca^{2+}$ | 100 | 79.08 | 42.79 | 4.17 |
| $Mg^{2+}$ | 100 | 76.22 | 42.25 | 3.94 |
| $Zn^{2+}$ | 100 | 74.55 | 41.78 | 3.75 |
| $Ni^{2+}$ | 100 | 73.65 | 40.65 | 3.68 |
| Mixed ions | Variable | 72.80 | 40.29 | 3.45 |

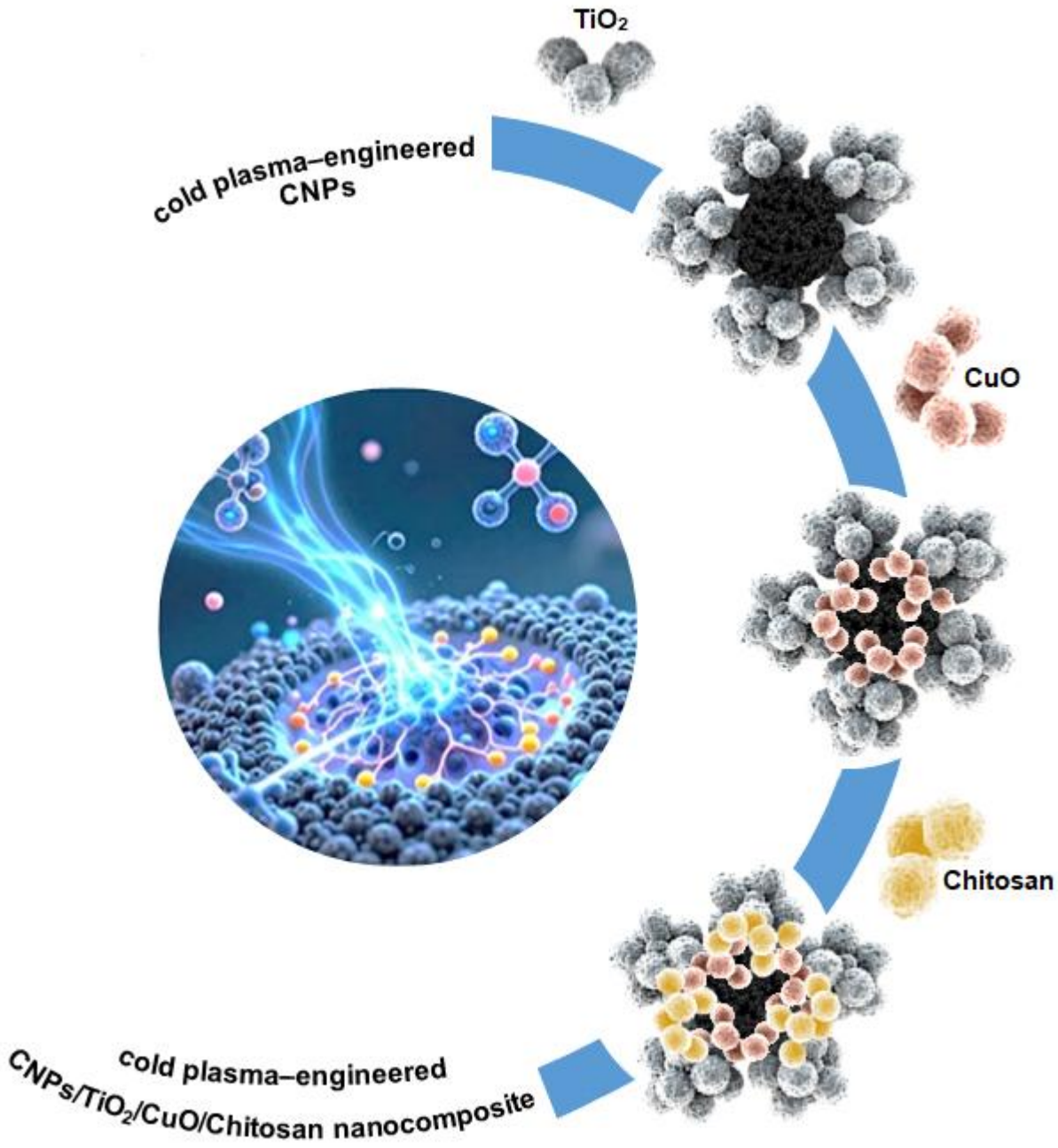

TiO2
cold plasma–engineered CNPs
CuO
Chitosan
cold plasma–engineered CNPs/TiO2/CuO/Chitosan nanocomposite

**Fig. 1**

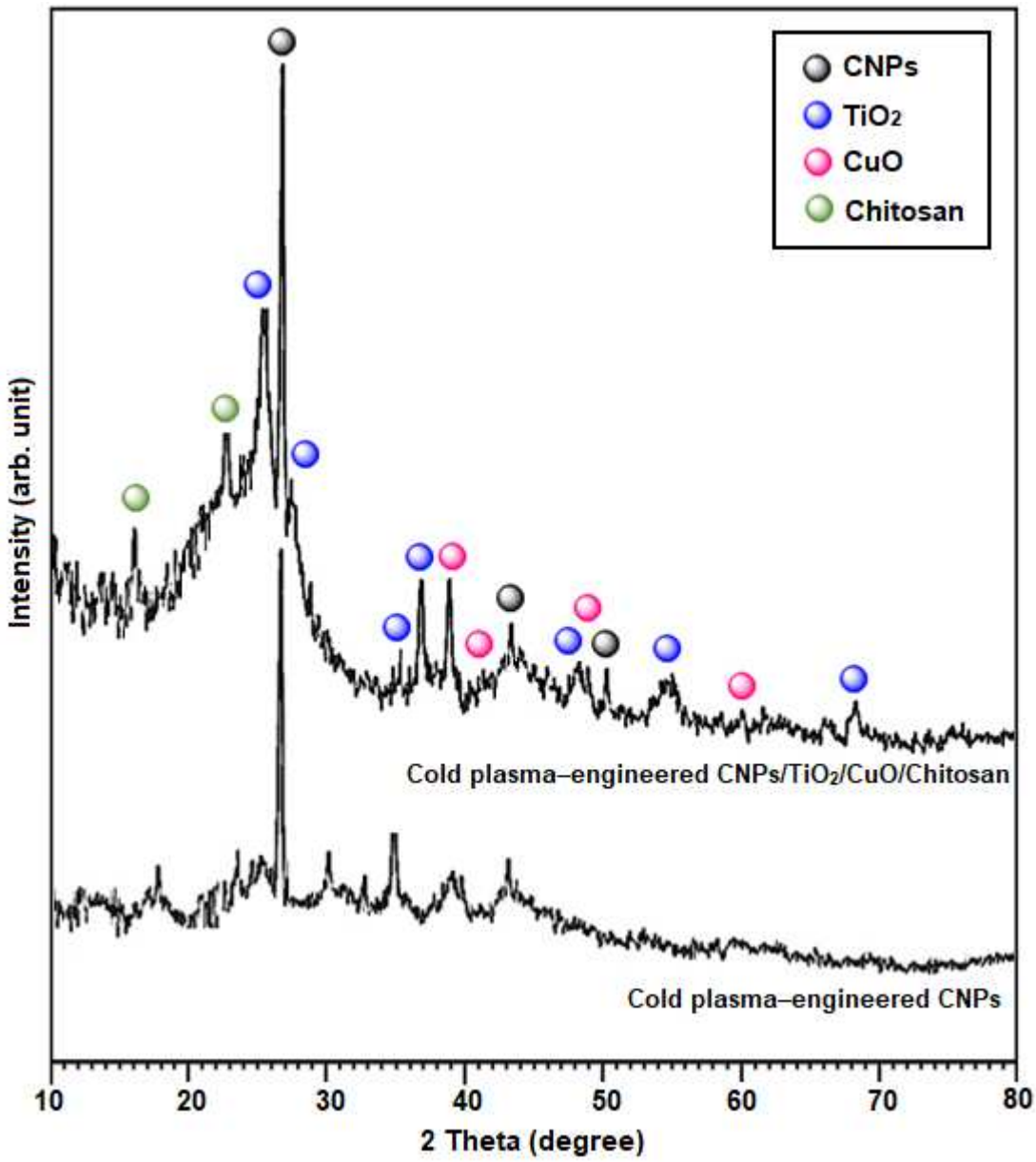

CNPs
TiO2
CuO
Chitosan
Intensity (arb. unit)
Cold plasma–engineered CNPs/TiO2/CuO/Chitosan
Cold plasma–engineered CNPs
10
20
30
40
50
60
70
80
2 Theta (degree)

**Fig. 2**

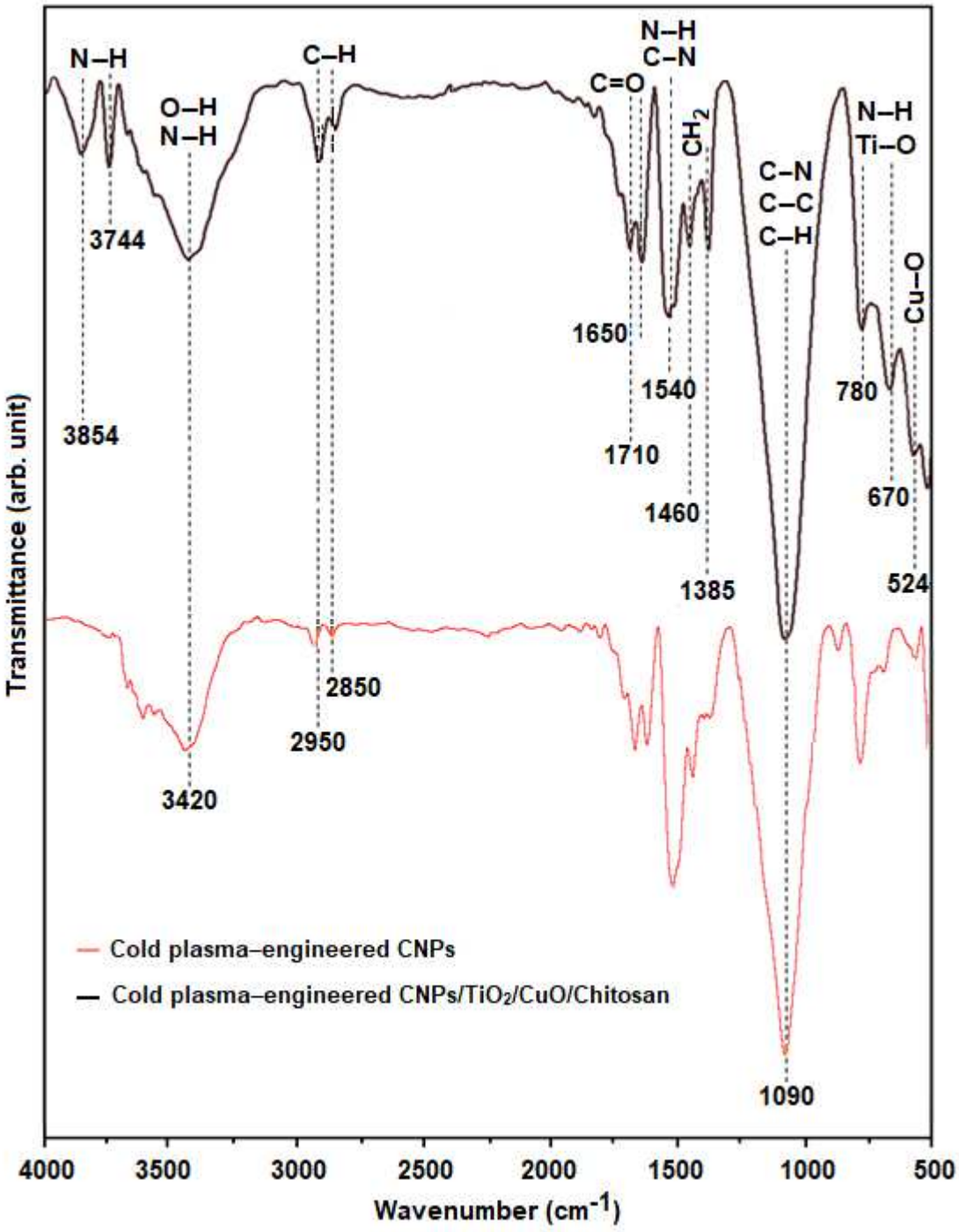

N–H
O–H
N–H
C–H
C=O
N–H
C–N
CH2
C–N
C–C
C–H
N–H
Ti–O
Cu–O
3744
3854
1650
1710
1540
1460
1385
1090
780
670
524
2850
2950
3420
Transmittance (arb. unit)
Cold plasma–engineered CNPs
Cold plasma–engineered CNPs/TiO2/CuO/Chitosan
4000
3500
3000
2500
2000
1500
1000
500
Wavenumber (cm-1)

**Fig. 3**

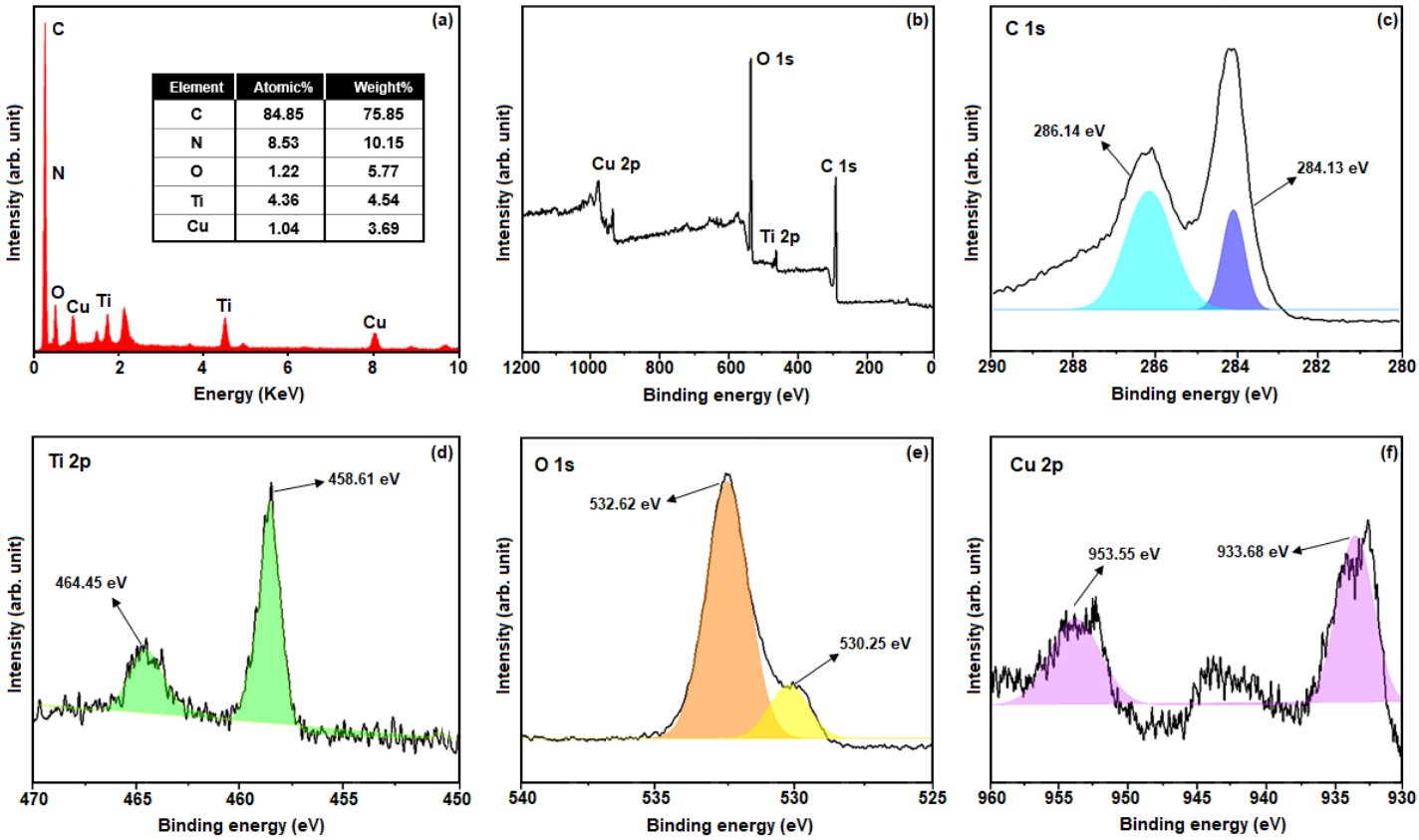

(a)
C
N
O
Cu
Ti
Ti
Cu
Intensity (arb. unit)
Energy (KeV)
Element | Atomic% | Weight%
C | 84.85 | 75.85
N | 8.53 | 10.15
O | 1.22 | 5.77
Ti | 4.36 | 4.54
Cu | 1.04 | 3.69
(b)
O 1s
Cu 2p
C 1s
Ti 2p
Intensity (arb. unit)
Binding energy (eV)
(c)
C 1s
286.14 eV
284.13 eV
Intensity (arb. unit)
Binding energy (eV)
(d)
Ti 2p
458.61 eV
464.45 eV
Intensity (arb. unit)
Binding energy (eV)
(e)
O 1s
532.62 eV
530.25 eV
Intensity (arb. unit)
Binding energy (eV)
(f)
Cu 2p
953.55 eV
933.68 eV
Intensity (arb. unit)
Binding energy (eV)

**Fig. 4**

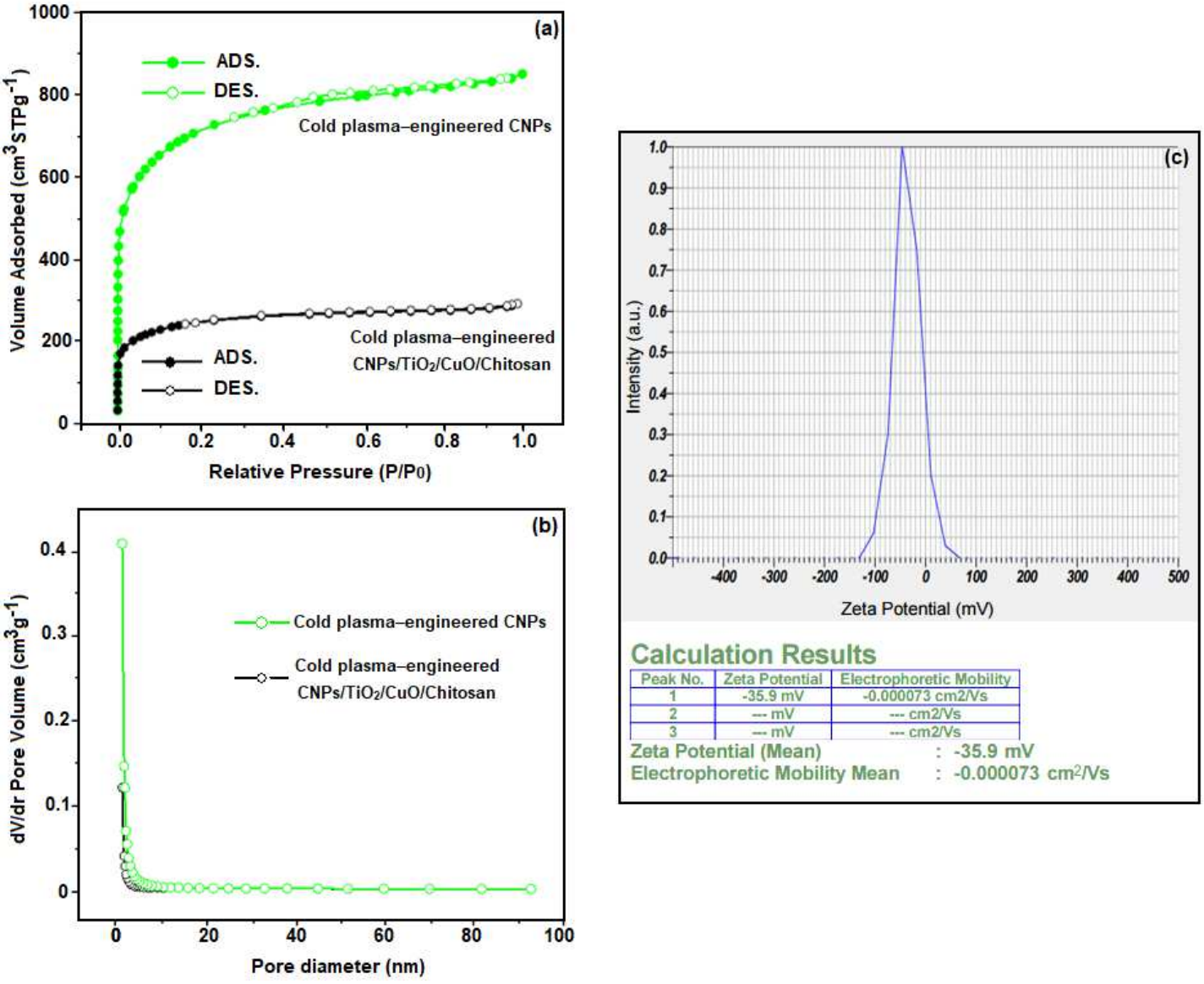

(a)
ADS.
DES.
Cold plasma–engineered CNPs
Cold plasma–engineered CNPs/TiO2/CuO/Chitosan
ADS.
DES.
Volume Adsorbed (cm3STPg-1)
Relative Pressure (P/P0)
(b)
Cold plasma–engineered CNPs
Cold plasma–engineered CNPs/TiO2/CuO/Chitosan
dV/dr Pore Volume (cm3g-1)
Pore diameter (nm)
(c)
Intensity (a.u.)
Zeta Potential (mV)
Calculation Results
Peak No. | Zeta Potential | Electrophoretic Mobility
1 | -35.9 mV | -0.000073 cm2/Vs
2 | --- mV | --- cm2/Vs
3 | --- mV | --- cm2/Vs
Zeta Potential (Mean) : -35.9 mV
Electrophoretic Mobility Mean : -0.000073 cm2/Vs

**Fig. 5**

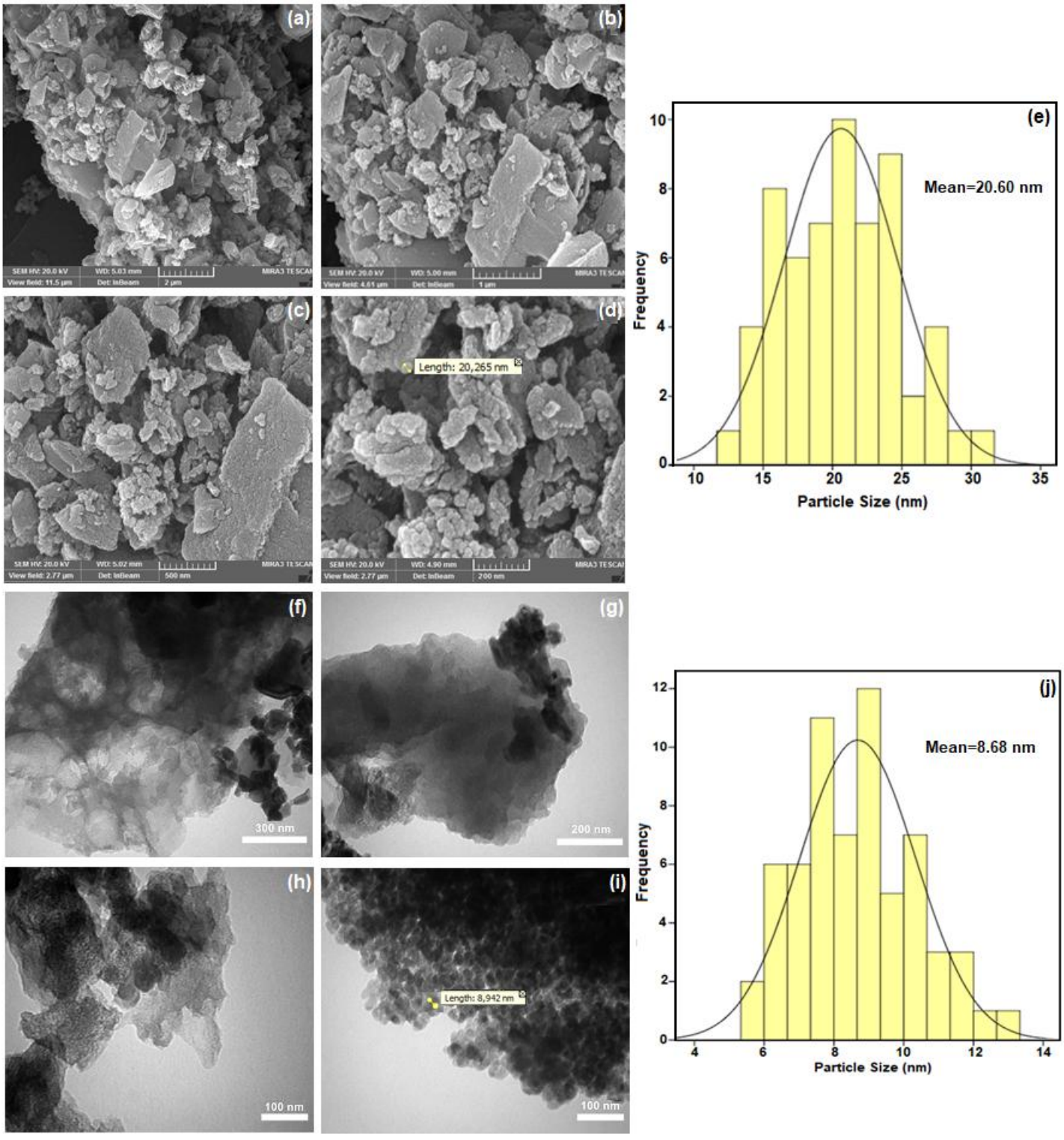

(a)
(b)
(c)
(d)
Length: 20,265 nm
(e)
Mean=20.60 nm
Frequency
Particle Size (nm)
(f)
300 nm
(g)
200 nm
(h)
100 nm
(i)
Length: 8,942 nm
100 nm
(j)
Mean=8.68 nm
Frequency
Particle Size (nm)

**Fig. 6**

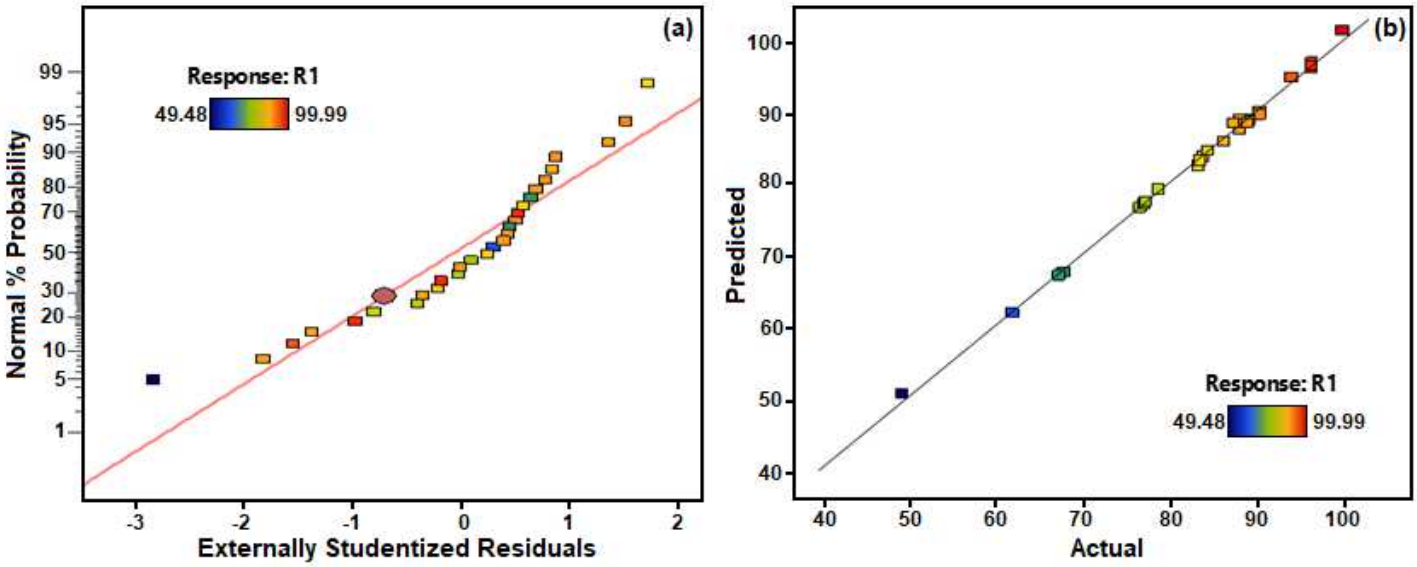

(a)
Response: R1
49.48
99.99
Normal % Probability
99
95
90
80
70
50
30
20
10
5
1
-3
-2
-1
0
1
2
Externally Studentized Residuals
(b)
Predicted
100
90
80
70
60
50
40
Response: R1
49.48
99.99
40
50
60
70
80
90
100
Actual

**Fig. 7**

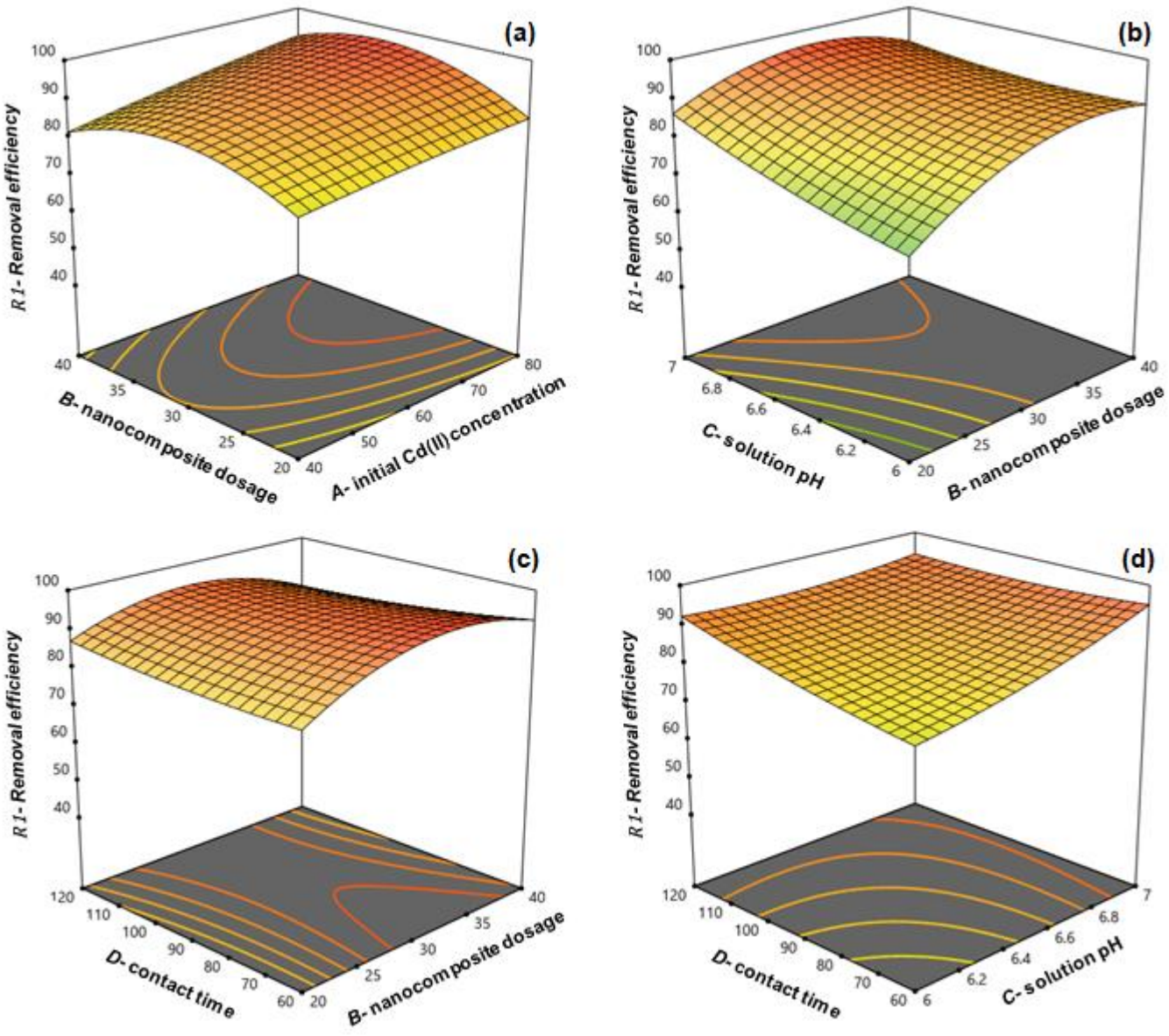

(a)
R1- Removal efficiency
100
90
80
70
60
50
40
B- nanocomposite dosage
40
35
30
25
20
A- initial Cd(II) concentration
40
50
60
70
80
(b)
R1- Removal efficiency
C- solution pH
7
6.8
6.6
6.4
6.2
6
B- nanocomposite dosage
20
25
30
35
40
(c)
R1- Removal efficiency
D- contact time
120
110
100
90
80
70
60
B- nanocomposite dosage
20
25
30
35
40
(d)
R1- Removal efficiency
D- contact time
120
110
100
90
80
70
60
C- solution pH
6
6.2
6.4
6.6
6.8
7

**Fig. 8**

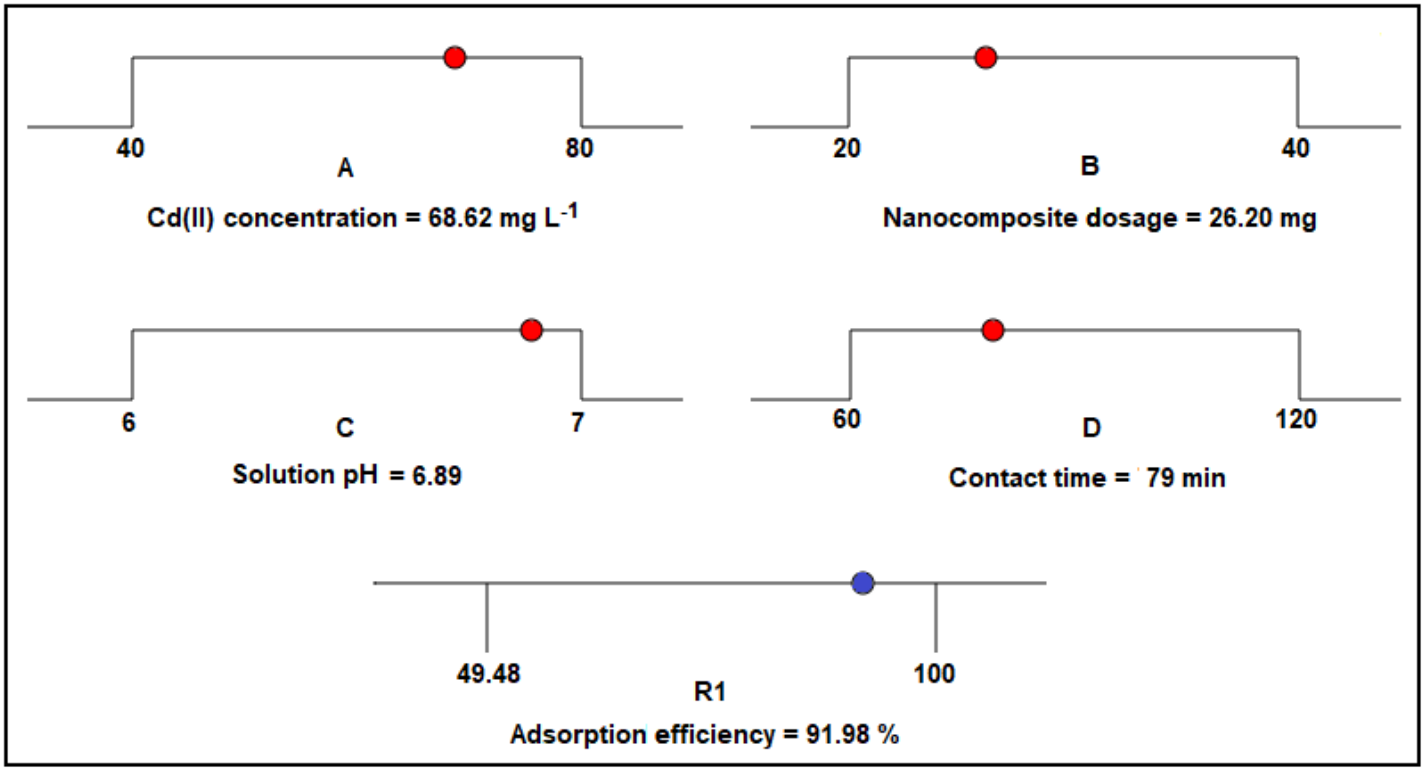

40
A
80
Cd(II) concentration = 68.62 mg L-1
20
B
40
Nanocomposite dosage = 26.20 mg
6
C
7
Solution pH = 6.89
60
D
120
Contact time = 79 min
49.48
R1
100
Adsorption efficiency = 91.98 %

**Fig. 9**

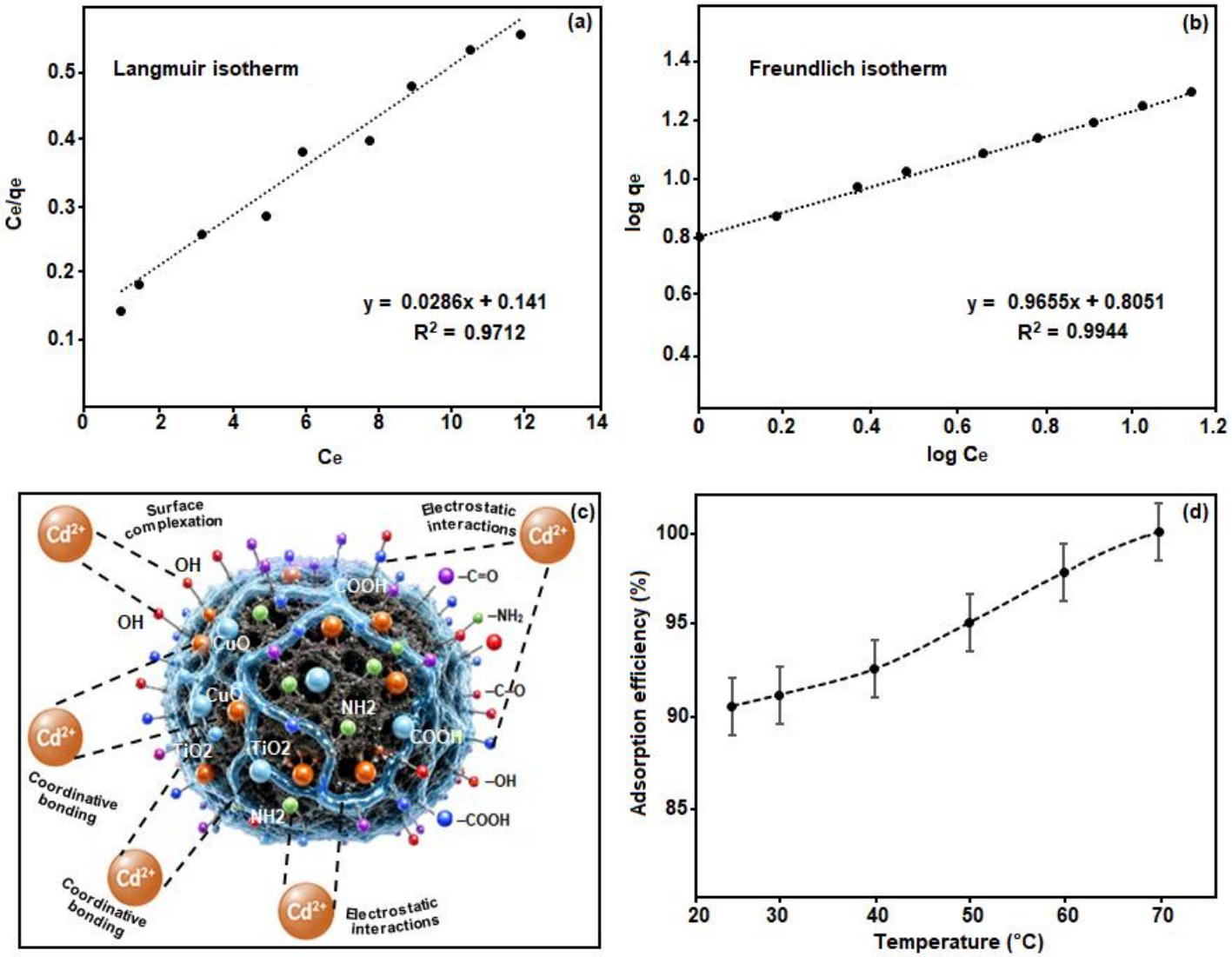

(a)
Langmuir isotherm
Ce/qe
Ce
y = 0.0286x + 0.141
R2 = 0.9712
(b)
Freundlich isotherm
log qe
log Ce
y = 0.9655x + 0.8051
R2 = 0.9944
(c)
Surface complexation
Electrostatic interactions
Cd2+
OH
COOH
–C=O
–NH2
CuO
NH2
–C–O
TiO2
–OH
–COOH
Coordinative bonding
Electrostatic interactions
(d)
Adsorption efficiency (%)
Temperature (°C)

**Fig. 10**

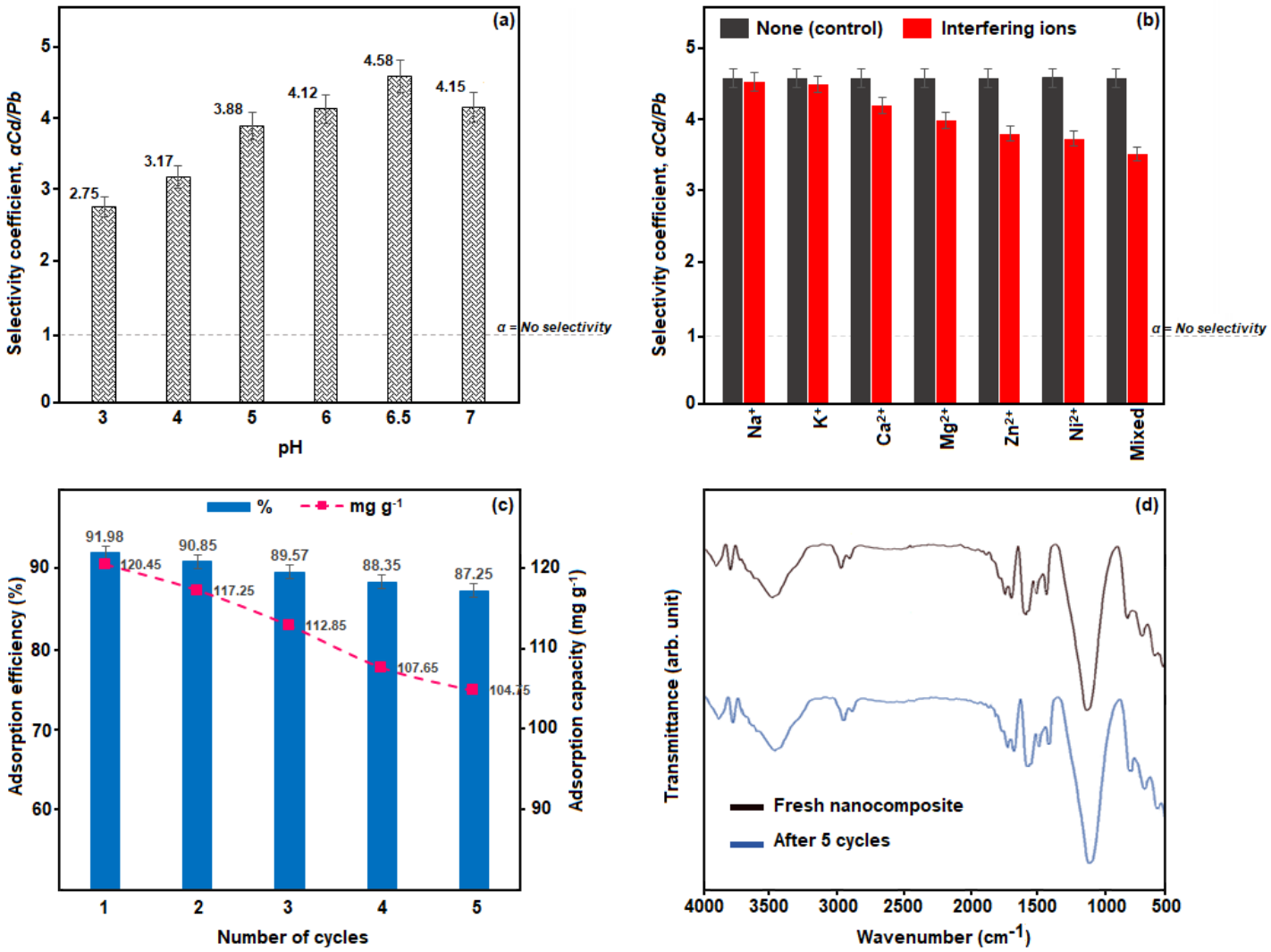

(a)
Selectivity coefficient, αCd/Pb
2.75
3.17
3.88
4.12
4.58
4.15
α = No selectivity
pH
(b)
None (control)
Interfering ions
Selectivity coefficient, αCd/Pb
α = No selectivity
Na+
K+
Ca2+
Mg2+
Zn2+
Ni2+
Mixed
(c)
%
mg g-1
Adsorption efficiency (%)
Adsorption capacity (mg g-1)
91.98
90.85
89.57
88.35
87.25
120.45
117.25
112.85
107.65
104.25
Number of cycles
(d)
Transmittance (arb. unit)
Fresh nanocomposite
After 5 cycles
Wavenumber (cm-1)

**Fig. 11**